Degree Project in Chemical Engineering
Second cycle, 30 credits

Coke Characteristics and Oxidation Kinetics on Spent Methylcyclohexane Dehydrogenation Catalysts

A Study Towards Efficient Hydrogen Delivery Using Liquid Organic Hydrogen Carriers

ISA PETTERSSON HAAG

TRITA-CBH-GRU-2025:205
Stockholm, Sweden 2025

www.kth.se

Abstract

Liquid organic hydrogen carriers (LOHC), such as the methylcyclohexane (MCH) – toluene (TOL) system, are emerging as an alternative solution to hydrogen storage and transport. However, the rapid catalyst deactivation due to coke deposition during MCH dehydrogenation is a major limitation for its development. Restoring the catalytic activity requires exothermic coke oxidation, which entails the risk of hotspots formation that can potentially damage both the catalyst and reactor. In this thesis, the oxidation behaviour of coke on spent platinum- (4 wt% Pt/γ-Al_2O_3 and 4 wt% Pt/$MgAl_2O_4$) and nickel-based (12 wt% Ni/γ-Al_2O_3 and 12 wt% Ni/$MgAl_2O_4$) catalysts, used in MCH dehydrogenation, is investigated.
The spent catalysts were analysed by temperature-programmed oxidation (TPO). Limited information from the TPO, combined with rapid deactivation, led to the decision not to investigate the Ni-based catalysts further. The Pt catalysts were analysed by means of thermogravimetric analysis (TGA), infrared spectroscopy (FTIR), and Soxhlet extraction followed by gas chromatography/mass spectrometry (GC/MS). Total carbon content on the catalysts was found to be 5.93 wt% and 6.81 wt% after 30 and 124 hours on stream for the Pt/Al_2O_3 and Pt/$MgAl_2O_4$ catalysts, respectively. Two oxidation events could be distinguished for the Pt-based catalysts, plausibly corresponding to coke on the metal and on the support. The coke on the Al_2O_3 support was found to be more dehydrogenated (H/C = 0.60 compared to 0.86 on Pt/$MgAl_2O_4$). This could be attributed to the higher acidity of the Al_2O_3 support, contributing to secondary reactions. The FTIR showed the presence of polyaromatic coke on Pt/Al_2O_3, correlating well with the determined H/C ratio. In addition, alkene, aromatic, and methyl group vibrations could be identified on the coked Pt/$MgAl_2O_4$ catalyst. However, similar peaks are also found in the reduced catalyst sample, indicating that further analysis is required to determine the exact nature of the coke. Moreover, TGA exhibited poor reproducibility, while Soxhlet extraction of Pt/Al_2O_3 revealed the presence of dimethylbiphenyls.

Furthermore, a kinetic model was developed to estimate kinetic parameters and simulate the regeneration taking into account different coke families, characterized by their oxidation reactivity. The activation energies were estimated to be 46.54 ± 0.50 kJ/mol and 68.78 ± 2.47 kJ/mol for the two coke families present on Pt/Al_2O_3 and 53.68 ± 0.79 kJ/mol and 43.52 ± 0.78 kJ/mol for those on Pt/$MgAl_2O_4$. Simulation of the regeneration showed that the coke on the $MgAl_2O_4$ support could be removed more readily than the coke on the Al_2O_3 support.

Keywords: LOHC, Methylcyclohexane dehydrogenation, Coke oxidation, Kinetic modelling, Catalyst regeneration

Sammanfattning

Flytande organiska vätgasbärare (LOHC), så som metylcyklohexan (MCH) – toluen (TOL) systemet, utvecklas som en alternativ lösning för vätgaslagring och transport. En stor begränsning i dess utveckling är dock den snabba katalysator-deaktiveringen orsakad av koksdeposition. Återställning av katalysatorns aktivitet kräver exoterm koksoxidation, vilket medför risk för uppkomsten av värmevågor som potentiellt kan leda till skada på både katalysatorn och reaktorn. Därför syftar denna avhandling till att undersöka oxidationsbeteendet hos koks på förbrukade platina- (4wt% Pt/γ-Al_2O_3 och 4wt% Pt/$MgAl_2O_4$) och nickel-baserade (12wt% Ni/γ-Al_2O_3 och 12wt% Ni/$MgAl_2O_4$) katalysatorer som deaktiverats genom MCH dehydrogenering.
De förbrukade katalysatorerna analyserades med temperaturprogrammerad oxidation (TPO). Begränsad information från TPO-analysen, i kombination med snabb deaktivering, ledde till att Ni katalysatorerna inte studerades vidare. Pt-katalysatorerna undersöktes dock vidare med termogravimetrisk analys (TGA), infrarödspektroskopi (FTIR) och Soxhlet-extraktion följt av gaskromatografi/masspektrometri (GC/MS). Den totala kolhalten på katalysatorerna befanns vara 5,93 wt% efter 30 timmar reaktionstid för Pt/Al_2O_3 respektive 6,81 wt% efter 124 timmar reaktionstid för Pt/$MgAl_2O_4$. Dessutom kunde två oxidations-event urskiljas för Pt-baserade katalysatorerna, troligtvis motsvarande koks på metallen och bärarmaterialet. Kokset på Al_2O_3-bäraren visade sig mer dehydrogenerat (H/C = 0,60 jämfört med 0,86 på Pt/MgAl2O4). Detta kan förklaras av den högre surheten hos Al_2O_3-bäraren vilket gynnar sekundära reaktioner. FTIR-analysen visade förekomst av polyaromatiskt koks på Pt/Al_2O_3, vilket korrelerar väl med det uppmätta H/C-förhållandet. Vidare så kunde vibrationer från alkener, aromater och metylgrupper identifieras på Pt/$MgAl_2O_4$-katalysatorn. Dessa toppar återfanns dock även i den reducerade katalysatorn och därmed krävs ytterligare analyser för att fastställa koksens exakta natur. TGA-mätningarna visade på låg reproducerbarhet, och Soxhlet-extraktion av Pt/Al_2O_3 påvisade förekomst av dimetylbifenyl föreningar.

En kinetisk modell utvecklades dessutom för att estimera kinetiska parametrar och simulera regenereringen genom att ta hänsyn till olika koksfamiljer vilka kan karakteriseras av sin oxidations reaktivitet. Aktiveringsenergierna uppskattades till $46{,}54 \pm 0{,}50$ kJ/mol respektive $68{,}78 \pm 2{,}47$ kJ/mol för de två koksfamiljerna på Pt/Al_2O_3 samt till $53{,}68 \pm 0{,}79$ kJ/mol respektive $43{,}52 \pm 0{,}78$ kJ/mol för motsvarande koks familjer på Pt/$MgAl_2O_4$. Simulering av regenereringen visade att kokset på $MgAl_2O_4$-bäraren kunde avlägsnas lättare än kokset på Al_2O_3-bäraren.

Keywords: Flytande organiska vätgasbärare, Metylcyklohexan dehydrogenering, Koks oxidation, Kinetisk modellering, Katalysatorregenerering

Acknowledgments

I want to express my gratitude to my supervisor and examiner, Efthymios, for all his guidance and feedback throughout this project. Thank you for always being available to help and for all the additional things you have taught me. I would also like to give my deepest thanks to my supervisor, Pol, for all his help and support, and thank you for making this project possible. Lastly, I would like to thank everyone in the department for being kind and welcoming.

Contents

List of Figures

List of Tables

List of Abbreviations

DTG	Derivative thermogravimetry
FTIR	Fourier-transform infrared spectroscopy
GC-MS	Gas chromatography/mass spectrometry
LHSV	Liquid hourly space velocity
LOHC	Liquid organic hydrogen carrier
MFC	Mass flow controller
MS	Mass spectrometer
PDH	Propane dehydrogenation
TGA	Thermogravimetric analysis
TOS	Time on stream
TPO	Temperature-programmed oxidation

List of Symbols

T	Temperature [K]
r	Reaction rate $[mol \cdot m^{-3} \cdot s^{-1}]$
R	Particle radius $[m]$
k_c	Mass transfer coefficient $[m/s]$
Sc	Schmidt number [-]
Re	Reynolds number [-]
D_{AB}	Diffusion coefficient $[m^2 \cdot s^{-1}]$
A	Cross-sectional area of the reactor $[m^2]$
L	Bed length [m]
d_p	Particle diameter [m]
d_t	Reactor diameter [m]
E_a	Activation energy $[kJ \cdot mol^{-1}]$
k_{ref}	Rate constant at reference temperature $[m^3 \cdot mol^{-1} s^{-1}]$
q	Volumetric flow rate $[m^3 \cdot s^{-1}]$
C_b	Bulk concentration $[mol \cdot m^{-3}]$
C_s	Concentration at particle surface $[mol \cdot m^{-3}]$
C_{O_2}	Oxygen concentration $[mol \cdot m^{-3}]$
C_{CO_2}	Carbon dioxide concentration $[mol \cdot m^{-3}]$
$C_{\text{H}_2\text{O}}$	Water concentration $[mol \cdot m^{-3}]$
$C_{\text{CH}m_j}$	Coke concentration, family j $[mol \cdot m^{-3}]$
D_e	Effective diffusivity $[m^2 \cdot s^{-1}]$
M_R	Mears criterion number [-]
WP	Weisz–Prater criterion number [-]
Pe	Péclet number [-]
n_r	Reaction order [-]
N_{coke}	Number of coke families
r'_{obs}	Observed reaction rate $[mol \cdot kg^{-1} \cdot s^{-1}]$
V_{pores}	Pore volume $[cm^3 \cdot g^{-1}]$

Greek letters

ρ_b	Bulk density $[kg \cdot m^{-3}]$
ρ_c	Catalyst density $[kg \cdot m^{-3}]$
ρ_{cat}	Catalyst material density $[g \cdot cm^{-3}]$
ρ_g	Gas density $[kg \cdot m^{-3}]$
μ_g	Gas dynamic viscosity $[kg \cdot m^{-1} \cdot s^{-1}]$
ν_z	Superficial axial velocity $[m \cdot s^{-1}]$
ϵ	Bed porosity [-]
ϵ_p	Particle porosity [-]
β	Linear heating rate $[K \cdot s^{-1}]$
τ	Tortuosity factor [-]

1. Introduction

The use of fossil fuels for energy production releases substantial amounts of greenhouse gas emissions, inevitably contributing to global warming and climate change. Increasing the share of renewable energy and eliminating the reliance on fossil fuels is necessary to reduce global emissions and ultimately achieve carbon neutrality [1]. The intermittent nature of renewable sources such as wind and solar leads to difficulties balancing energy supply and demand. Thus, the development of energy transport and storage systems is a prerequisite for the transition to renewable energy [2]. Hydrogen is one of the most promising energy carriers due to its high gravimetric energy density and application in hydrogen-based energy systems, such as fuel cells [3]. There are however, major challenges regarding the storage of hydrogen. Hydrogen has a very low volumetric energy density, requiring large storage volumes under ambient conditions [4]. Alternative storage solutions such as highly compressed hydrogen gas or cryogenic liquid storage require large investments in infrastructure development and pose safety risks [4].

An emerging solution with the potential to overcome these challenges is liquid organic hydrogen carriers (LOHC). A LOHC system consists of a pair of organic compounds, one saturated or hydrogen-rich, and one unsaturated or hydrogen-lean [5]. Hydrogen-lean LOHCs can chemically store hydrogen through double bond saturation, a reaction known as hydrogenation [4]. This allows hydrogen to be chemically stored in liquid form under ambient conditions, overcoming the problems associated with storage and transport of gaseous hydrogen [4]. In addition, the process is reversible and hydrogen can be released through a dehydrogenation reaction [5]. Moreover, since the LOHC carriers are not spent, they can be reused in further hydrogenation-dehydrogenation reactions, which enhances the circularity and sustainability of the LOHC system. The toluene (TOL) to methylcyclohexane (MCH) is among the most investigated LOHC systems [3]. In this system, TOL is hydrogenated into MCH, which can be stored or transported pending usage. The MCH is then dehydrogenated, producing TOL and hydrogen. However, one of the great challenges in the TOL/MCH system is that the dehydrogenation reaction requires elevated temperatures due to its endothermic nature, which in turn leads to the formation of side products and catalyst deactivation through coking [5]. The coking mechanism is, to some extent, reversible, and the catalytic activity can be restored through a regeneration process in which the coke is oxidized. However, the exothermic nature of coke oxidation can lead to the development of large heat waves or hot spots, potentially damaging both catalyst and reactor [6]. Understanding the formation and oxidation behavior of coke is therefore essential to mitigate these risks and to enable efficient regeneration.

1.1 Aim and Objectives

As outlined above, the dehydrogenation reaction and associated coke deposition introduce major challenges for the implementation of LOHC systems for hydrogen transport and storage. Understanding the coke composition and catalyst regeneration by oxidation is crucial for the operability of the MCH dehydrogenation process. Therefore, this thesis aims to study the regeneration and oxidation behavior of coke on spent catalysts used in the dehydrogenation of MCH. The objectives pursued in this thesis include studying the oxidation behavior through temperature-programmed oxidation and the development of a kinetic model to simulate the transient oxidation of multiple coke species. The model is used for the estimation of kinetic parameters and simulation of the regeneration process. In addition, coke characterization is attempted using thermogravimetric analysis, infrared spectroscopy, and Soxhlet extraction combined with gas chromatography/mass spectrometry.

2. Background

2.1 Methylcyclohexane Dehydrogenation

Methylcyclohexane (MCH) is a methyl-substituted cycloalkane, which upon dehydrogenation is converted to toluene (TOL) through the release of three hydrogen molecules, see Fig. 1. The TOL retains its aromatic structure and can be hydrogenated, regenerating MCH and thus enabling hydrogen storage.

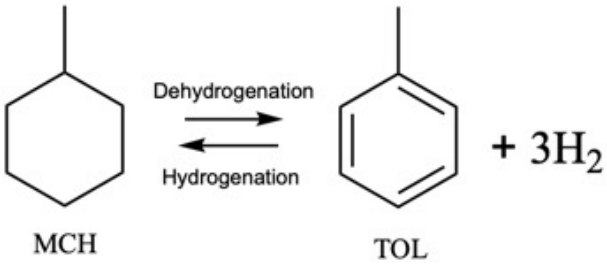

Figure 1: Hydrogenation-dehydrogenation cycle for MCH/TOL

Moreover, MCH is favored for hydrogen storage for multiple reasons. It has low volatility, low toxicity, and high theoretical hydrogen storage capacity (6.22 wt%) [7][8]. However, the MCH dehydrogenation reaction is very slow and requires catalysts to improve reaction kinetics [7]. The dehydrogenation of MCH to TOL releases hydrogen through the reversible and endothermic reaction [9], shown in Eq. (1).

$$C_7H_{14} \rightleftharpoons C_7H_8 + 3H_2, \quad \Delta H^{\circ}_{298K} = 204.8 \text{kJ/mol} \tag{1}$$

Because MCH dehydrogenation is endothermic, elevated temperatures are needed to shift equilibrium to the products [7]. Consequently, the reaction is typically run in the gas phase over heterogeneous catalysts [10]. Catalysts play a vital role in the MCH dehydrogenation reaction and control both dehydrogenation activity and product selectivity [11]. Supported metal catalysts are common for MCH dehydrogenation, where the active metal is dispersed on a catalyst support. In the literature, a variety of active noble metals have been investigated such as Pt, Pd, Ir, and Rh [7]. Among these, Pt is the most investigated due to its excellent ability to activate C-H bonds without breaking C-C bonds [7]. However, the scarcity and high cost of noble metals have driven extensive research into non-noble alternatives [7]. Transition metals such as Ni, Cu, Zn and Mo exhibit promising dehydrogenation performance, and Ni-based catalysts in particular have been extensively explored [10][12]. In addition to the active metal itself, factors such as morphology, metal-support interactions, and the acidity of the support influence the catalyst activity and stability [11].

The actual reaction mechanism does not occur in a single step, as expressed in Eq. (1), but rather through a series of dehydrogenation steps. In each step, a hydrogen atom is removed through the cleavage of a C-H bond, leading to the formation of a C=C double bond [8]. The MCH dehydrogenation reaction is also prone to a number of side reactions

reducing MCH conversion and product selectivity. Alhumaidan et al [13] investigated the possible side reactions of MCH dehydrogenation over Pt/Al_2O_3. According to their study, the byproducts could be divided into two categories: byproducts derived from MCH, and byproducts derived from TOL. With MCH as the precursor, the main byproducts were methylcyclohexene, paraffins and substituted-cyclopentanes. The main byproducts derived from TOL were benzene, xylene, and a variety of substituted-biphenyls [13]. Furthermore, methylcyclohexene has been reported to be formed by partial dehydrogenation, paraffins through ring-opening reactions, and substituted-cyclopentanes either through paraffin cyclization or ring-opening and ring-closing reactions of methylcyclohexene [13]. In terms of the TOL-derived byproducts, it has been described that benzene and xylene can form through TOL disproportionation. Benzene can also form through demethylation which is common on highly active Pt sites. Lastly, substituted-biphenyls have been described to form through condensation reactions between TOL or benzene molecules [13]. Over time, many of these byproducts can undergo further dehydrogenation, condensation, and polymerization reactions, ultimately forming carbonaceous deposits on the catalyst surface, also referred to as coke.

2.2 Deactivation by Coking

Coking refers to the physical deposition of carbonaceous species, or coke, on the surface of the catalyst [14]. Blocking of pores and active sites by coke deposits can result in loss of activity, thus deactivating the catalyst over time [14]. Coking can sometimes involve the chemisorption of hydrocarbons on the catalyst surface, contributing to catalyst deactivation by poisoning [14]. A general mechanism for coke formation does not exist, but its formation is often described to occur through a series of reactions such as dehydrogenation, condensation, polymerization and cyclization, depending on the catalytic system and reactions involved [15]. In addition, the chemical nature of coke is often described as arbitrary and difficult to define since its formation is very dependent on the feed, reaction conditions, and the catalyst properties [16][17]. However, coke is generally described to include everything from heavy hydrocarbons, often aliphatic or aromatic in nature, to graphitic carbon [18].

Coke can be formed both at the metallic active sites as well as on the support [16][19]. As the coke precursors form on the metal, they can migrate to the support and undergo condensation and polymerization reactions, aided by the acidic function of the support [15][18]. For this reason, the coke on the support is usually more dehydrogenated with a lower hydrogen-to-carbon (H/C) ratio compared to the coke on the metal [15][18]. Although it is commonly accepted that more coke formation leads to higher deactivation, nonetheless, the opposite has also been found. Kumar et al. [20] reported that the addition of Sn to Pt/SBA-15 catalysts used for propane dehydrogenation gave improved activity and stability despite increased coke formation. Increased migration of coke from the active sites to the support was attributed as the main cause of the effect.

2.3 Coke Oxidation and Regeneration

Coking is a reversible type of deactivation where the catalytic activity can be restored through a regeneration process [6]. In most industrial catalytic processes, coke is oxidized in the presence of oxygen [21]. However, coke oxidation is an exothermic reaction which can lead to the development of large heat waves or hot spots [6] [21]. The development of heat waves is of great concern since they can damage both the catalyst and the reactor, and hence it becomes essential to study the oxidation behavior and reactivity of the coke.

Establishing the temperature at which coke is oxidized can also provide information about the location of the coke on the catalyst particle. The oxidation behavior can be studied using tools such as thermogravimetric analysis (TGA) and temperature-programmed oxidation (TPO), which are further described in section 2.4. It has been described in the literature that coke oxidation at lower temperatures can be attributed to coke located on or near the metal, while coke burning at higher temperatures can be attributed to the coke on the support [19][22][23]. However, there does not appear to be any consensus in the literature on the exact temperature considered to be low and high in the context of coke oxidation, and instead it appears to be relative to the overall oxidation window. Wang et al. [22] investigated the coke deposited on Pt-Sn/Al_2O_3 catalyst used for propane dehydrogenation (PDH). They identified two oxidation regions, the lower at 400–500 °C, which was attributed to the coke on the metal, and the higher at 500–600 °C, which was attributed to the coke on the support. Moreover, the coke formation by PDH over Pt-Sn/SBA-16 catalysts has been investigated by Ruelas-Leyva et al. [23]. Their results revealed two oxidation regions, a lower around 240 °C, attributed to the coke on the metal, and a higher around 460 °C, attributed to the coke on the support. The two coke types were referred to as "soft" and "hard" coke. Similarly, Li et al. [19] investigated PDH over Pt-Sn/Al_2O_3 and found coke oxidation at intervals 150–280 °C and 380–430 °C. They also ascribed their lower and higher regions to the coke on the metal and support. Consequently, the oxidation temperature for a certain coke depends not only on the catalytic system and reactants, but also on the reaction conditions and the time on stream (TOS). Generally, the H/C ratio decreases with TOS, which means that coke becomes more graphitic in nature and less reactive, thus shifting the oxidation region to higher temperatures [18][22].

Furthermore, the influence of particle size for MCH dehydrogenation over Pt/Al_2O_3 has recently been investigated by Wu et al. [24]. The oxidation behavior of spent Pt-based catalysts with 0.05, 0.1 and 1 wt% Pt-loading was studied, and the results showed that the ratio between the coke on the metal and support varied with the metal loading. The oxidation profile for 1 wt% Pt exhibited a large peak at 580 °C, together with a shoulder peak at around 350 °C. Decreasing the Pt loading to 0.1 wt% shifted and lowered the intensity of the high temperature peak to around 550 °C and increased the intensity of the low temperature shoulder. Lastly, for the 0.05 wt%Pt sample, only one large oxidation peak at around 410 °C could be observed. The merging of the high and low oxidation peaks was attributed to this effect, indicating lower coke formation on the support and higher on the metal particles. Additionally, they observed higher deactivation for the 0.05 wt% Pt sample, compared to the others, but lower total coke formation, which could be explained by the larger amount of coke on the Pt active sites for the 0.05 wt% Pt sample.

2.4 Coke characterization

The complex coking reactions occurring on the catalyst can generate numerous coke species with varying composition [22]. To eventually understand these coking mechanisms and develop effective prevention strategies, it is important to first study the properties and the nature of the deposited coke.

2.4.1 Spectroscopic Analysis (Raman & FTIR)

Fourier Transform Infrared (FTIR) spectroscopy as well as Raman spectroscopy are characterization techniques utilized for qualitative analysis of coke. In Raman, two characteristic bands exist, the D and G bands, corresponding to the ring stretching in polyaromatic compounds [19]. The ratio between the D and G band gives a sort of measure of the graphitization of coke, where a high ratio indicates a low degree of graphitization, making Raman a common and useful method for coke characterization [19][23]. FTIR can provide similar information on the presence of aliphatic and aromatic species on the catalyst [22]. However, overlapping peak areas and limited information on the coke compositions might complicate the spectral analysis [19].

2.4.2 Thermal Analysis (TGA & TPO)

TGA and TPO both utilize a temperature program to oxidize coke in a predominantly inert atmosphere with limited oxygen supply. The TGA instrument measures the weight loss of the sample and is often used to quantify the total amount of coke present on a catalyst [18][22]. Additionally, it is possible to determine the derivative of the TG curve (DTG) and thereby obtain the oxidation profile of the coke. However, the TPO records the oxidation products from the outlet stream, thus providing an oxidation profile from the carbon dioxide (CO_2) and carbon monoxide (CO) production [24]. In addition to the CO_2 production, it is possible to obtain information about the water (H_2O) production and the oxygen (O_2) consumption.

2.4.3 Extraction and Gas-Chromatography

According to literature, the more hydrogen-rich, or soft coke, can be dissolved in a suitable solvent, thus enabling compositional analysis [25]. Soxhlet extraction is a continuous liquid-solid extraction technique performed under ambient pressure and can be used to extract the soluble fraction of coke [26]. Analytical techniques such as gas chromatography-mass spectrometry(GC-MS) can subsequently be used for compositional analysis of the extract [25] [27]. Afonso et al. [25] performed Soxhlet extraction of a coked Pt-Sn/Al_2O_3 catalyst used for the conversion of n-alkenes to mono-olefins. A sequential extraction was conducted using n-hexane, chloroform and TOL in addition to a single extraction using TOL only. Analysis of the extracts showed that the total amount of extracted coke remained unchanged when comparing the single and sequential extractions. Furthermore, the results indicated that hexene and chloroform were less efficient at extracting aromatics compared with TOL [25]. Furthermore, Van Doorn and Moulijn [27] conducted Soxhlet extraction on spent cobalt-molybdenum-based hydrotreating catalysts using dichloromethane, benzene and hexane, and their results showed that dichloromethane

and hexane were more suitable for coke extraction compared to benzene. The results also implied that the solubility of coke is dependent on the extraction procedure and that the suitability of an extraction medium might alter depending on the process and nature of the coke [27]. Sahoo et al [15] investigated the nature of coke deposited on spent Pt-Sn/Al_2O_3 catalysts used in the dehydrogenation of paraffins. Soxhlet extraction was performed using dichloromethane, and analysis of the extract indicated the presence of several polyaromatic compounds [15]. Furthermore, gas chromatography-mass spectrometry (GC-MS) is commonly used for compositional analysis of the extract [25] [27].

3. Methods

3.1 Materials

$Ni(NO_3)_2 \cdot 6H_2O$ (purity Ni $\geq$ 98.5%) and $[Pt(NH_3)_2]_4(NO_3)_2$ (purity Pt $\geq$ 99.995%) were used as metal precursors for the catalyst preparation and were supplied by Sigma Aldrich. Toluene ($C_6H_5CH_3$) AnalaR/NORMAPUR, Ph. Eur., ACS analytical reagent grade (CAS: 108-88-3) supplied by VWR International, was used as extracting solvent, while extraction thimble, 501 cellulose, Batch no. 1624, supplied by VWR European, was used in the Soxhlet extraction apparatus.

3.2 Catalyst Preparation and Deactivation

Four catalysts were prepared: two Pt-based, namely, 4 wt% Pt/γ-Al_2O_3 and 4 wt% Pt/$MgAl_2O_4$, and two Ni-based, 12 wt% Ni/γ-Al_2O_3 and 12 wt% Ni/$MgAl_2O_4$. The catalysts were prepared by dry impregnation. The Ni catalysts were prepared by sequential impregnation. After impregnation, the catalysts were dried at 80 °C for 24 h in air atmosphere and calcined at 500 °C for 5 h at a heating rate of 3 °C/min. The particle size for all catalysts was measured to be 100 μm on average. Prior to dehydrogenation, 2 g of catalyst was loaded into the reactor and reduced at 550 °C for 2 h, using a mixture of 10% H_2 in Ar, with a flow of 100 Nml/min. After reduction, the temperature was fixed at 320 °C and MCH was supplied at a liquid hourly space velocity (LHSV) of 2.2 h^-1 (0.1 ml/min) together with N_2 (590 Nml/min), at a pressure of 1.5 bar. The reaction proceeded until the activity had decreased by at least 90% in relation to the initial catalyst activity. The bulk density was measured to be 0.66 g/ml and 0.55 g/ml for the deactivated Pt/Al_2O_3 and Pt/$MgAl_2O_4$ catalysts, respectively.

3.3 Soxhlet Extraction and GC/MS

The coked Pt/Al_2O_3 sample was extracted with TOL in a Soxhlet extraction apparatus. For the extraction, approximately 0.5 g of catalyst was weighed and placed inside a cellulose thimble, which was placed inside the extraction chamber equipped with a siphon. A three-headed round-bottom flask was filled with approximately 100 ml of TOL solvent and put in a heating mantle. The flask was fitted with the Soxhlet extractor, a thermometer and an adapter connected to a nitrogen supply. The Soxhlet extractor was equipped with a reflux system, using glycol-based cooling liquid, and connected to a bubble meter. The heating was fixed around the solvent's boiling point during the whole extraction. The extraction was terminated after approximately 18 h, and the thimble was removed and dried in an oven at 115°C overnight. The extract was dried under vacuum to remove solvent and analyzed with an Agilent 7890B-5975MSD GC-MS system. A schematic illustration of the extraction apparatus can be seen in Fig. 2.

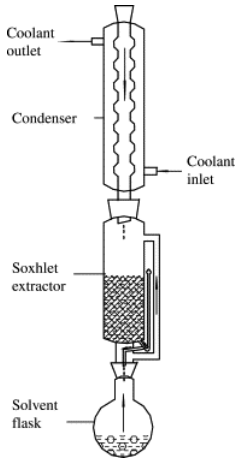

Figure 2: Soxhlet extraction apparatus [26]

3.4 Temperature programmed Oxidation (TPO)

The catalyst oxidation was conducted in an AutoChem 2910 (Micrometrics) instrument coupled with a GSD 350 Omnistar mass spectrometer (Pfeiffer). In the sample preparation, a U-tube reactor was loaded with glass wool and approximately 0.4 g of catalyst (fixed bed), and placed in the oven to dry at 115°C overnight. After drying, the catalyst weight was recorded and the U-tube was placed inside the TPO. The temperature was increased to 120 °C with a heating rate of 10 °C under argon (Ar) flow (50 Nml/min), and held at 120 °C for 30 min. The gases were then switched to 1% O_2 in Ar (50 Nml/min) and the system was purged for 2-4 min. Thereafter, the temperature was increased to 750 °C at a heating rate of 2 °C/min. TPO was performed on all catalyst samples; however, TPO measurements for the extracted samples failed due to leakage in the sample holder.

3.5 Thermogravimetric Analysis (TGA)

TGA was conducted in a STA 449 F3 jupiter thermogravimetric analyzer (Netzsch). A crucible was loaded with approximately 30-40 mg of catalyst sample and placed in the TGA. The temperature was increased to 120 °C at a heating rate of 10 °C/min and then kept at 120 °C for 1 h under nitrogen (N_2) atmosphere (100 Nml/min). The temperature was then increased to 750°C with a heating rate of 1°C/min and in air atmosphere (20% O_2 in N_2 50ml/min), together with 50 Nml/min N_2 protective gas. TGA was performed on all Pt samples.

3.6 Spectroscopy

FTIR spectra were collected with a PerkinElmer FT-IR spectrometer with a resolution of 4 cm^{-1}. The analysis range was 4000 cm^{-1} to 400 cm^{-1}, and 50 scans were averaged for each spectrum. FTIR was performed on all Pt samples. Additionally, Raman spectroscopy was attempted on the coked catalyst using Confocal Raman Microscope Witec. Laser wavelengths of 400–785 nm were tested, however, no peaks were observed due to high fluorescence.

4. Model Development and Data Processing

This section presents the complete development of the kinetic model together with the parameter-estimation procedure. The model is based on the work by Sørensen, Martin Dan Palis [6], describing a coke-burning kinetic model for zeolite catalysts. Parameter estimation is performed using data obtained from the TPO experiments. Since these experiments did not detect CO, the kinetic model is developed considering only the formation of CO_2. The TPO results are presented and further discussed in section 5.1.3.

4.1 Reaction Expressions

The exact composition of coke species is difficult to establish using physical characterization methods. Instead, the coke can be categorized by its oxidation reactivity. For instance, coke on the metal and on the support usually differ in their reactivity and can therefore provide different oxidation profiles as discussed in section 2.3. Coke oxidizing within a certain temperature range can thus be considered as one reactive family. Each family is assumed to have a characteristic H/C ratio and is represented using the generalized coke formula CH_{mj} where j is the coke family and m is the H/C ratio. The generalized oxidation reaction is given in Eq. (2).

$$(CH_m)_j + (1 + \frac{m_j}{4}O_2) \rightarrow CO_2 + \frac{m_j}{2}H_2O, \quad j = 1, 2, \ldots, N_{\text{Coke}} \tag{2}$$

Furthermore, the reaction rate for each family is assumed to be first order with respect to coke and O_2 concentrations, see Eq. (3).

$$r_j = -k_j C_{CH_{mj}} C_{O_2} \tag{3}$$

The reaction rate coefficient, k_j, can be described by the temperature-dependent Arrhenius equation. However, to reduce correlation between the parameters in the Arrhenius equation, it can be reparameterized using a reference temperature, see Eq. (4) [28]. The topic of parameter correlation is discussed in Section 4.5.1.

$$k_j(T) = k_{j,ref} e^{\frac{E_{a_j}}{R}(\frac{1}{T_{j,ref}} - \frac{1}{T})} \tag{4}$$

Where $k_{j,ref}$ is the reaction rate coefficient at a certain reference temperature $T_{j,ref}$, E_{a_j} is the activation energy and R is the gas constant. The reference temperature for a certain coke family can be determined through the inverse average, according to Eq. (5).

$$\frac{1}{T_{j,ref}} = \frac{1}{NE}\sum_{p=1}^{NE}\frac{1}{T_j, p}, \quad p = 1, 2, \ldots, NE \tag{5}$$

Where NE is the number of measurements and $T_{j,p}$ is the temperature at each measurement point.

4.2 Reactor Model

The oxidation is performed using a finite amount of coke and follows a temperature-dependent program where the outlet concentrations vary with time, resulting in a non-steady state (dynamic) operation. To simplify the model, the assumption of ideal plug flow can be adopted, assuming that there are no temperature, concentration, and velocity gradients in the radial direction and no dispersion in the axial direction [29]. In order to minimize wall- and dispersion effects and approach plug flow in a packed bed, the following criteria must be fulfilled [29]:

$$\frac{L}{d_p} > 50 \tag{6a}$$

$$\frac{d_t}{d_p} > 10 \tag{6b}$$

Where d_t is the reactor tube diameter, d_p is the particle diameter and L is the length of the bed. The assumption of negligible dispersion was experimentally verified with tracer tests and is presented in section 5.2.1. Furthermore, a slow heating rate, in addition to a small amount of coked catalyst and low O_2 concentration, ensures that the extent of reaction remains low at any given time, resulting in minimal heat generation which ensures that the isothermal bed and particle assumptions are satisfied. For these reasons, the reactor can be assumed to operate under isothermal conditions. Additionally, the co-feeding of inert gas together with O_2 allows for increased heat removal [29]. Moreover, the intrinsic kinetic parameters can only be determined if the reaction is not limited by external mass transfer or internal diffusion limitations. To verify that the coke oxidation is kinetically controlled, the Mears (MR) and Weisz-Prater (WP) criteria were calculated. External mass transfer limitations can be neglected if the MR < 0.15, see Eq. (7) [30].

$$MR = \frac{r'_{obs}\rho_b R n_r}{k_c C_b} \tag{7}$$

Where r'_{obs} is the observed reaction rate, ρ_b is the bulk density, R is the particle radius, n_r is the reaction order, C_b is the bulk concentration, and k_c is the mass transfer coefficient. Internal diffusion limitations can be neglected if WP $\ll 1$, see Eq. (8).

$$WP = \frac{r'_{obs}\rho_c R^2}{D_e C_s} \tag{8}$$

Where ρ_c is the catalyst density, C_s is the concentration at the particle surface, which can be considered as C_b if there are no external mass transfer limitations, and D_e is the effective diffusivity, see Appendix A for a complete set of equations. Furthermore, based on the stated assumptions, the solid phase balance can be defined according to Eq. (9).

$$\frac{\partial C_{(CH_m)_j}}{\partial t} = r_j \tag{9}$$

Where r_j is the reaction rate for family j. Assuming that the coke families are uniformly distributed in the reactor, the initial coke concentration for each family can be described according to the following:

$$C_{CH_{mj}}(0, z) = C^{\circ}_{CH_{mj}}(z) \tag{10}$$

Furthermore, assuming that concentrations only varies in the axial direction, the gas phase balances can be described according to the partial differential equations (PDE) presented in Eq. (11)-(13).

$$\epsilon\frac{\partial C_{O_2}}{\partial t} = -\nu_z\frac{\partial C_{O_2}}{\partial z} + (1-\epsilon)\sum_{j=1}^{N_{coke}}(1+\frac{mj}{4})r_j \tag{11}$$

$$\epsilon\frac{\partial C_{CO_2}}{\partial t} = -\nu_z\frac{\partial C_{CO_2}}{\partial z} - (1-\epsilon)\sum_{j=1}^{N_{coke}} r_j \tag{12}$$

$$\epsilon\frac{\partial C_{H_2O}}{\partial t} = -\nu_z\frac{\partial C_{H_2O}}{\partial z} - (1-\epsilon)\sum_{j=1}^{N_{coke}} r_j \tag{13}$$

Where v_z is the superficial velocity and ϵ is the bed porosity. Since the PDEs are of first order, boundary conditions (at z=0) and initial conditions (at t=0) are required. Purging the system with the oxidation gas mixture (1% O_2 in Ar) before the start of the reaction gives an initial condition of O_2. The initial conditions for H_2O and CO_2, on the other hand, are equal to zero at the start of the reaction. The initial conditions for the gas phase species are found in Eq. (14a)-(14b).

$$C_{O_2}(0,z) = C^{\circ}_{O_2} \tag{14a}$$

$$C_s(0,z) = 0, \quad s = CO_2, H_2O \tag{14b}$$

Furthermore, the boundary conditions at the inlet (z=0) are presented in Eq. (15a)-(15b).

$$C_{O_2}(t,0) = C^{\circ}_{O_2} \tag{15a}$$

$$C_s(t,0) = 0, \quad s = CO_2, H_2O \tag{15b}$$

Moreover, the porosity in packed beds is given by Eq. (16) [31].

$$\epsilon = 0.38 + 0.073[1 + \frac{(d_t/d_p - 2)^2}{(d_t/d_p)^2}] \tag{16}$$

Where d_t is the tube diameter and d_p is the equivalent particle diameter. Assuming ideal gas, negligible pressure changes, and constant total molar flows due to mainly inert flow (99% Ar), the temperature-dependent superficial velocity can be expressed according to Eq. (17).

$$\nu_z = \nu_{z0}(\frac{T_0 + \beta t}{T(\nu_{z0})}) \tag{17}$$

Where ν_{z0} is the inlet superficial velocity reordered at the mass flow controller (MFC), $T(\nu_{z0})$ is the temperature at the MFC, T_0 is the initial temperature of the ramp and β is the heating rate.

4.3 Experimental Data Processing

The MS peaks were numerically integrated and the peak area signals for each gas species were internally calibrated against Ar. All numerical integrations were done using Simpson's rule. Furthermore, a polynomial baseline was subtracted for the O_2 profile, and the CO_2 evolution profile was numerically integrated to find the total carbon amount. The TPO curves for CO_2 and O_2 were deconvoluted, based on the oxidation profile and number of coke families, using the Trust-Region algorithm. Each deconvoluted peak was numerically integrated, and the H/C ratio could be calculated for each coke according to Eq. 18.

$$m_j = \frac{4(n_{O_2,j} - n_{CO_2,j})}{n_{CO_2,j}} \tag{18}$$

Where $n_{O_2,j}$ and $n_{CO_2,j}$ is the moles of O_2 and CO_2 for coke family j.

4.4 Discretization

The gas phase balances presented in Eq. (11)-(13) form a system of coupled nonlinear PDEs. A common approach to solving time-dependent PDEs is to use the method of lines (MoL) [32]. The MoL uses finite differences (FD) to discretize spatial derivatives while keeping the time derivatives, and thus, the MoL is referred to as a semi-discrete method. The spatial derivatives can be approximated by various FDs. Upwind FDs are commonly used in convection-dominated problems due to their unconditional numerical stability [33]. In Eq. (19) the first order space derivative is approximated using the upwind scheme.

$$\frac{\partial C_i}{\partial z} = \frac{C_i - C_{i-1}}{h}, \quad i = 1, 2..., n, \quad h = \frac{L}{n} \tag{19}$$

Where, n is the number of points in space and h is the distance between each point. Semi-discretization allows the PDE system to be transformed into a system of ordinary differential equations (ODE). In the original study conducted by Sørensen, Martin Dan Palis [6], the author used explicit Runge-Kutta to solve the system of ODEs and ensured numerical stability via the Courant–Friedrichs–Lewy condition (CFL). In contrast, the current work uses the ode15s solver in MATLAB, which uses implicit numerical differentiation formulas [34]. Because ode15s is an implicit solver is not restricted by the CFL condition and remains stable for large time steps. However, although the solver is unconditionally stable, it might lose accuracy if excessively large time steps are used [35]. In addition, the number of mesh-points was set to 50, which provided a mesh-independent solution. Mesh independence tests were performed and can be found in Appendix B.

4.5 Parameter Estimation

The parameter estimation is performed using experimental data from the TPO together with the dynamic model in which a finite set of unknown parameters appears. The

parameters to be estimated in this work are k_{ref} and E_a for each coke family which enters the model through the Arrhenius equation (Eq.(4)). The mathematical model can be represented according to the following expression:

$$y^{calc} = f(x, \theta) \tag{20}$$

Where f is the function defining the coupled system of ODEs, x is the experimental time data, θ is the vector of unknown parameters and y^{calc} is the model response. The parameter estimation approach is usually based on the minimization of an objective function. The objective function, $O(\theta)$, can be written as the sum of squared residuals, see Eq. (21).

$$O(\theta) = \sum_{i=1}^{N_{data}} (y_{CO_2}^{meas,i} - y_{CO_2}^{calc,i})^2 \tag{21}$$

Where N_{data} is the number of experimental points and where $y_{CO_2}^{calc,i}$ is evaluated at the outlet (z=L). The objective function is not weighted due to the concentrations of CO_2 reaching values of zero in the experimental data. Furthermore, the minimization of the objective function was carried out using the trust-region algorithm. This algorithm is gradient based, meaning that it can be sensitive to noisy data [36]. In addition, it is possible for the solver to get stuck at local minima and thus it is important to verify a solution with different initial guesses.

4.5.1 Parameter Correlation

The Arrhenius equation is commonly used to describe the temperature dependence of reaction rates in chemical reactions and is usually written according to Eq. (22).

$$k = A^{\frac{-Ea}{RT}} \tag{22}$$

Where A is the pre-exponential factor and E_a is the activation energy. It is common to estimate the Arrhenius parameters, A and E_a, from experimental data. However, due to the mathematical structure of the Arrhenius equation, it introduces a strong dependence between the parameters [28]. This dependence is referred to as parameter correlation. A high parameter correlation means that several combinations of A and E_a can be used to describe the experimental data (compensation effect), and consequently, the physical interpretation of the parameters becomes unreliable. To minimize correlation between the parameters, it is common to reparameterize the Arrhenius equation by introducing a reference temperature, as seen in the reparameterized Arrhenius in Eq (4). The choice of reference temperature can strongly affect the correlation and it is common to either use the average temperature or the inverse average (Eq. (5)) [37]. Furthermore, if the Arrhenius parameters are estimated based on experimental data, it is possible to evaluate the parameters through calculation of the correlation. Correlation values close to 1 or -1 would indicate strong correlation, while a correlation closer to zero indicates a lower degree of correlation [37].

5. Results & Discussion

This section presents the experimental and modeling results. First, the catalyst performance and coke characterization results are presented and discussed, followed by the peak deconvolution, parameter estimation, and simulation of the regeneration process.

5.1 Catalytic Activity and Coke characterization

5.1.1 Catalyst Deactivation

The goal with the dehydrogenation was to deactivate the catalyst under realistic conditions and reach a sufficiently high degree of deactivation in order to study the coke. For this reason, the TOS varies for all catalysts. The relative activities for $Pt/MgAl_2O_4$ and Pt/Al_2O_3 are plotted against TOS in Fig. 3.

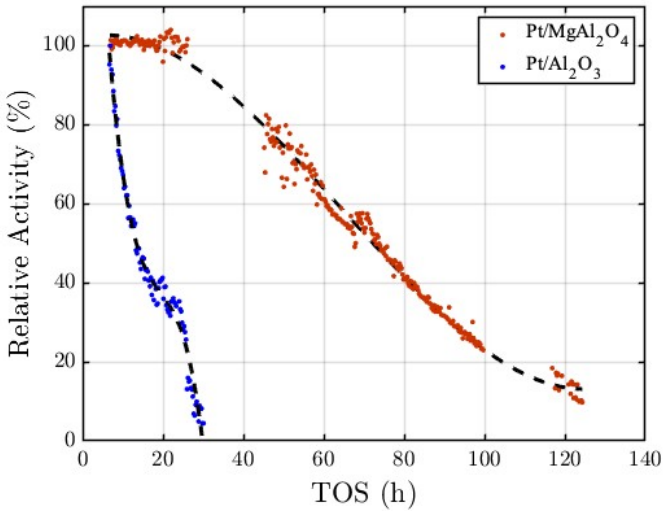

Figure 3: Normalized activity over TOS for Pt/Al_2O_3 and $Pt/MgAl_2O_4$

It can be observed in Fig. 3 that the deactivation of Pt/Al_2O_3 occurs more rapidly in comparison to $Pt/MgAl_2O_4$. For Pt/Al_2O_3 the activity displays a sharp decline from the start, which then tapers off after around 15 h on stream, before undergoing a further drop in activity. An overnight shutdown followed by a restart at around 20 h TOS likely caused the change in slope observed in the activity profile. During the shutdown, the feeding was paused, but the catalyst was kept under N_2 at 150 °C. The reaction was terminated after 30 h on stream when a relative activity of around 4.5% could be measured. $Pt/MgAl_2O_4$ displays a different behavior where the activity is initially stable and continues to decrease at a lower overall decrease rate. The activity then tapers off after around 100 h on stream, and the reaction was terminated after 124 h on stream at a relative activity of 9.7%. Furthermore, it should be noted in Fig. 3 that the gaps in the activity measurements for the $Pt/MgAl_2O_4$ correspond to times when the TCD measurements were turned off but the reactions were still running.

The pronounced variation in deactivation behavior indicates that the catalysts undergo coking via different mechanisms.

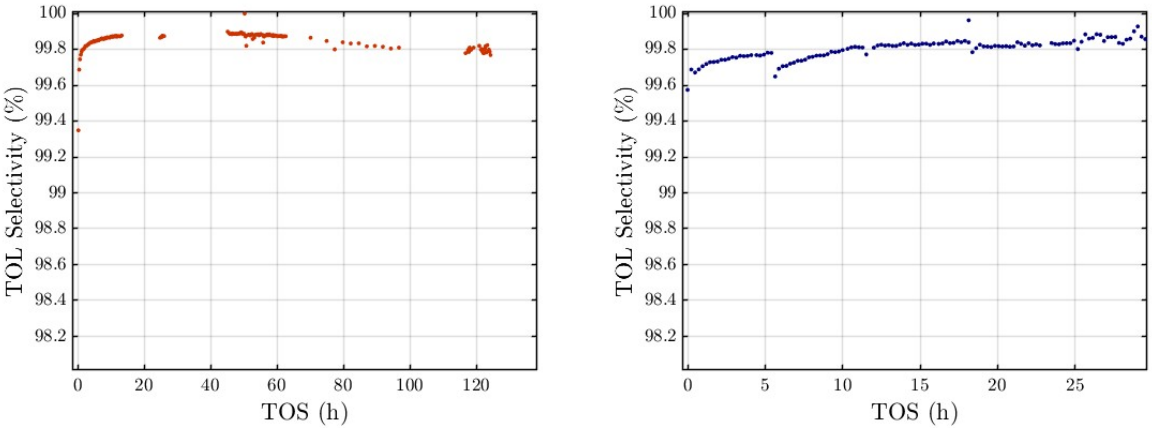

Figure 4: TOL selectivity over TOS for (a) $Pt/MgAl_2O_4$ and (b) Pt/Al_2O_3

In the dehydrogenation reaction, byproducts from isomerization, cracking, and cyclization reactions were detected but found to be far below ppm levels. Therefore, these compounds were neglected and a representative indication of selectivity was considered, see Eq.(23)

$$Selectivity(\%) = \frac{Toluene}{Toluene + Benzene} \cdot 100 \tag{23}$$

The MCH selectivity is plotted against time for the Pt samples in Fig. 4. It can be seen in Fig. 4 that the selectivity remains high for both catalysts over the reaction, which is beneficial for higher product yield. The drops in the selectivity for Pt/Al_2O_3 can be attributed temporary termination of the reaction. Both catalysts also display an initial selectivity increase at the start of the run. Similar behavior has been observed for propane dehydrogenation over Pt catalysts [23]. The effect can be explained by the active sites for side-reactions being coked faster, thus increasing selectivity for the desired reaction [23]. Noteworthy, the Ni/Al_2O_3 and $Ni/MgAl_2O_4$ samples deactivated much faster, with a TOS of 4h and 4.5h, respectively. Due to their fast deactivation and measurement fluctuations, these samples are not presented.

5.1.2 Soxhlet Extraction and GC-MS

The extraction was only performed on Pt/Al_2O_3. The extracted catalyst was sent to TPO and TGA analysis, but unfortunately, the TPO measurement failed due to leakage in the sample holder. The TGA results are presented in section 5.1.5. Furthermore, the extract was analyzed using GC-MS, and the results indicated contamination from soap or vaseline due to the presence of long-chain fatty acids and alcohols, see the full chromatogram in Appendix C. However, several regioisomeric dimethylbiphenyls could be found, which are common byproducts derived from TOL and are considered coke precursors [13]. In summary, no heavier coke species could be found in the extract, indicating that the coke was not soluble or that their concentration was too low for detection.

5.1.3 Temperature programmed Oxidation (TPO)

All catalyst samples were further analyzed using TPO by measuring evolved gases. In Fig. 5a, the CO_2 and H_2O evolutions are shown for Pt/Al_2O_3, along with the consumption of O_2. Fig. 5b displays the TPO profile for all the evolved gases. All signals have been normalized against Ar.

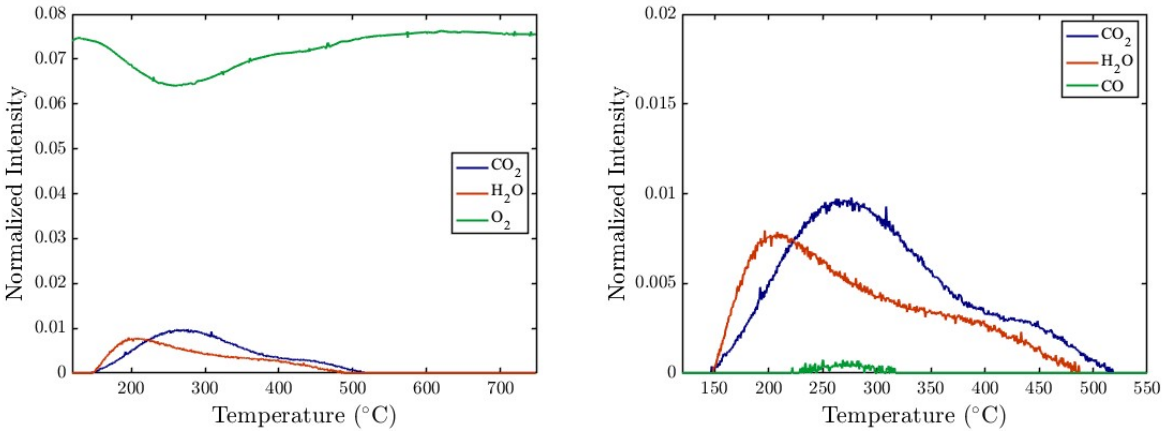

(a) (b)

Figure 5: TPO profiles of spent Pt/Al_2O_3

It can be observed in Fig. 5a that the CO_2 formation and O_2 consumption curves are of similar shape, clearly indicating the existence of coke oxidation. A closer inspection of the evolved gases in 5b, shows that the CO_2 formation is dominating, with a very low CO signal detected. The observed CO signal could originate from fragmentation of CO_2 into CO in the MS, which is known to occur at a ratio of approximately 9.8% [38]. Therefore, the CO detected can be attributed to this effect. The absence of detected CO from the oxidation of coke is likely due to CO oxidation over Pt, which is especially probable since Pt catalysts are commonly used for CO oxidation [39]. In the simplest mechanism, CO and O_2 adsorb on the Pt surface and react following the Langmuir–Hinshelwood mechanism, resulting in the formation of CO_2 [39]. However, other alternative reaction mechanisms are also possible [39]. For these reasons, the CO formation will not be considered in the analysis or modeling of Pt catalysts.

Furthermore, the CO_2 peak in Fig. 5b displays a large oxidation peak centered at 270°C along with a shoulder peak at around 427 °C. The presence of two peaks indicates two types of coke with different reactivity. The main peak at 270 °C and the shoulder peak at 427 °C could be assigned to the coke on the Pt metal and Al_2O_3 support, respectively. In this case, the TPO profile would indicate that the majority of the coke is located on the metal rather than the support. In Fig. 5b one can also observe that the shape of the H_2O peak is similar to that of CO_2 with a larger peak followed by a shoulder peak, further confirming two oxidation regions. Additionally, the H_2O peak is slightly shifted to the left, suggesting that the H reacts more easily compared to carbon. One possible explanation is that the coke might become further dehydrogenated (with the released H_2 subsequently being oxidized) in the TPO, thus reducing the H/C-ratio of the remaining coke. Additionally, part of the H_2O formed at lower temperatures could correspond to adsorbed water being released. Moreover, the total carbon

amount in the coke was determined using numerical integration and found to be 5.93 wt%.

Moreover, the TPO for spent $Pt/MgAl_2O_4$ catalyst is presented in Fig. 6. The TPO profile of $Pt/MgAl_2O_4$ is relatively similar to that of Pt/Al_2O_3 with a weak CO signal and H_2O drift to the left, which can be explained by the same artifacts as previously mentioned. However, the CO_2 signal in Fig. 6 exhibits a broad oxidation peak with its maximum around 275 °C and with an extended high-temperature tail. This could either be considered as one single oxidation peak with a tail produced by instrumental drifts, which would indicate that coke only formed on the metal and not on the support, resulting in a single coke reactivity. On the other hand, the oxidation behavior could also be explained as two oxidation peaks merging into what appears to be a single oxidation event. The presence of two oxidation peaks is not unlikely, considering the long TOS for this catalyst sample. Longer TOS increases the likelihood of coke deposition at different locations (metal and support) and for further reactions such as dehydrogenation and polymerization. For this reason, it is plausible that at least two coke oxidation reactivities are present for the $Pt/MgAl_2O_4$ catalyst. In addition, the CO_2 profile spans over a broad temperature range (150–500 °C), which is significantly broader than what is usually observed for a single oxidation peak. Comparison with the Pt/Al_2O_3 sample in Fig. 5, which shows two oxidation events within the same temperature range, supports the interpretation that the $Pt/MgAl_2O_4$ sample also exhibits two overlapping oxidation events. Furthermore, the total amount of carbon in the coke formed on $Pt/MgAl_2O_4$ was determined to be 6.81 wt%, which is slightly more than the 5.93 wt% carbon on the Pt/Al_2O_3. However, considering that the $Pt/MgAl_2O_4$ had a TOS of 124h compared to 30h for Pt/Al_2O_3, it becomes obvious that the $Pt/MgAl_2O_4$ is the superior catalyst for MCH dehydrogenation and that the overall coking rate is lower.

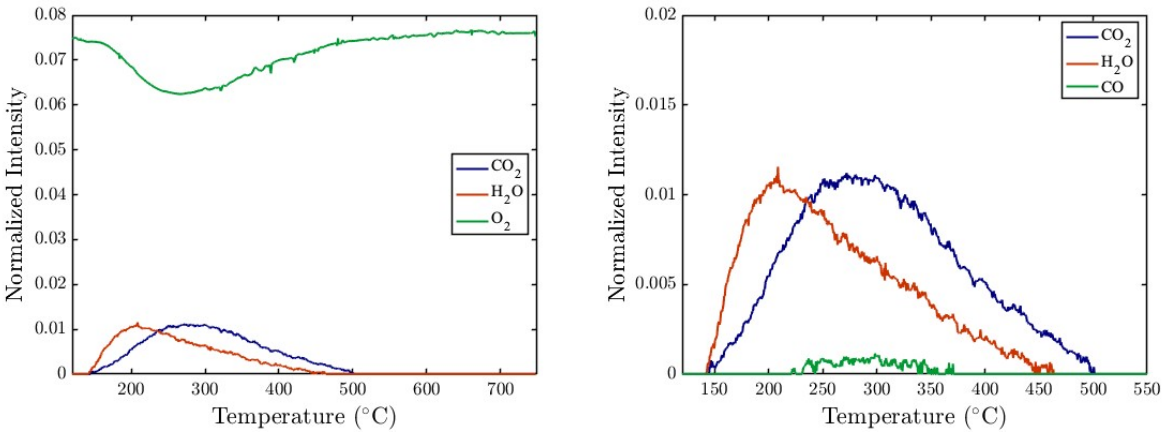

Figure 6: TPO profile of spent $Pt/MgAl_2O_4$

The total carbon content on the Ni catalysts was found to be 2.80 wt%, 3.67 wt% for the Ni/Al_2O_3 and $Ni/MgAl_2O_4$, respectively. This result indicates that despite the rapid deactivation of the Ni catalysts, less coke was formed. The carbon amount on all catalysts along with the TOS can be seen in Table 1. Furthermore, Fig. 7 depicts the TPO profiles for Ni/Al_2O_3 and $Ni/MgAl_2O_4$. No CO was detected for either catalyst sample. It is possible that the CO_2 fragmentation into CO was less since the total

Table 1: Total carbon on all catalyst and time-on-stream (TOS)

Catalyst	Carbon on catalyst (wt%)	TOS (h)
Pt/Al_2O_3	5.93	30
$Pt/MgAl_2O_4$	6.81	124
Ni/Al_2O_3	2.80	4
$Ni/MgAl_2O_4$	3.67	4.5

amount of coke was less. Additionally, the sample sizes were smaller for the Ni samples compared to the Pt samples, which is also reflected in the normalized intensity. The absence of CO could, similarly to the Pt samples, be explained by CO oxidation over Ni. According to literature, CO can be oxidized over a variety of Ni and Ni-oxide catalysts [40].

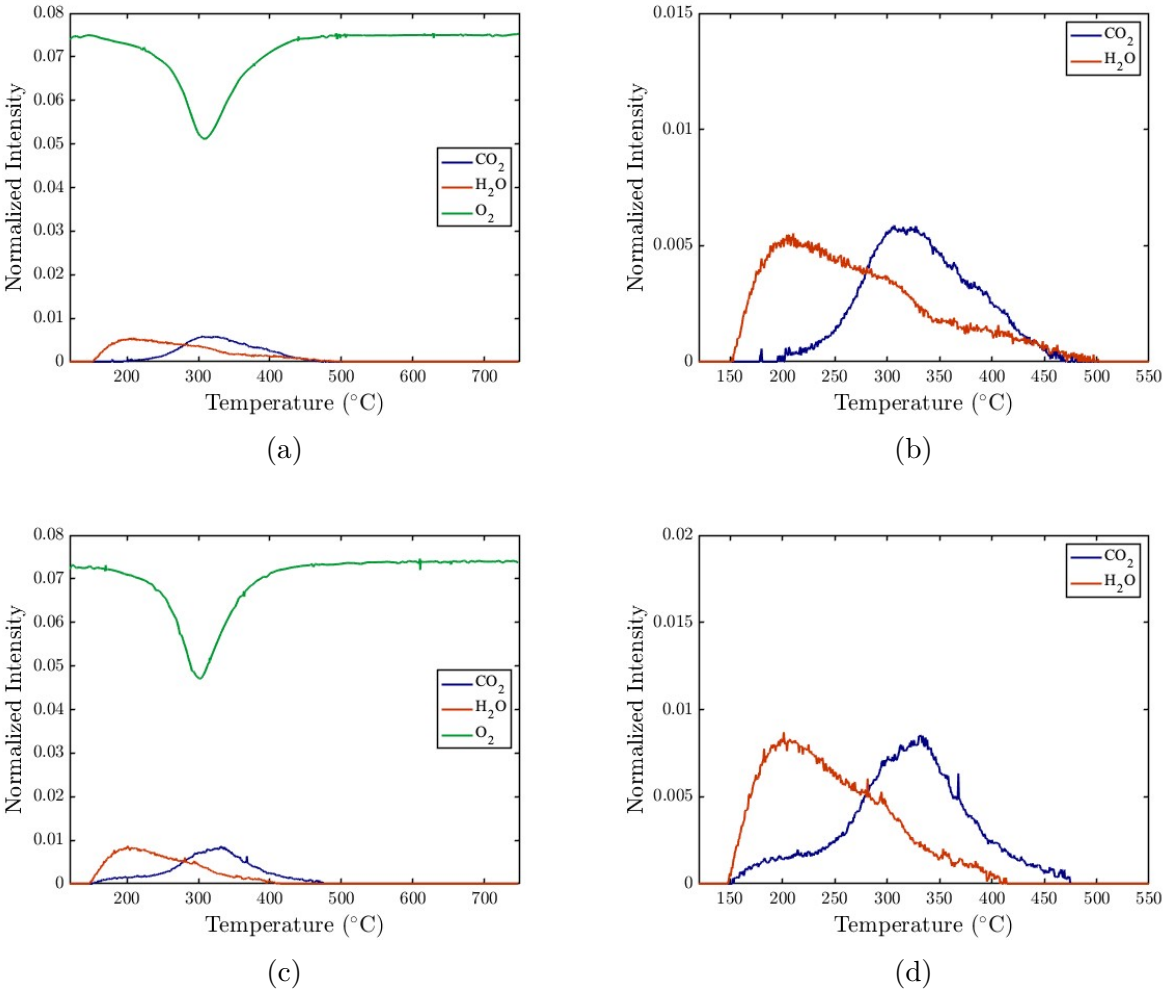

Figure 7: TPO profiles of spent (a)(b) Ni/Al_2O_3 and (c)(d) $Ni/MgAl_2O_4$

5.1.4 TPO Deconvolution

The TPO profiles for CO_2 evolution presented in section 5.1.3, were deconvoluted. The deconvolution for Pt/Al_2O_3 is displayed in Fig. 8.

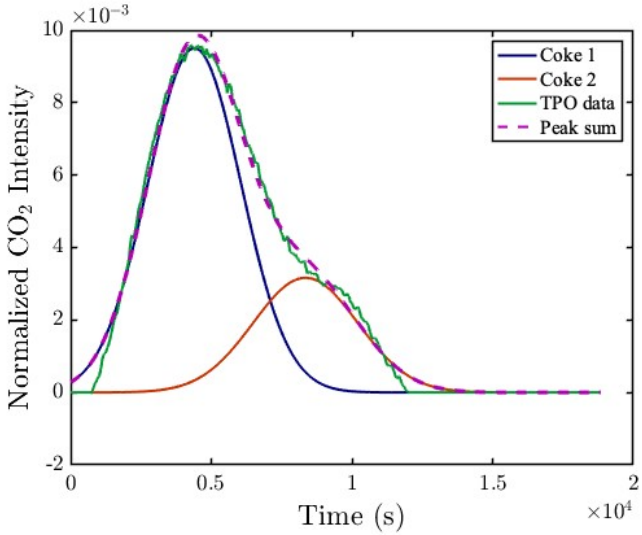

Figure 8: Deconvoluted CO_2 profile for Pt/Al_2O_3

It can be seen in Fig. 8 that the TPO profile can be described as the sum of two Gaussian curves, where each deconvoluted curve is considered a separate coke family with a certain reactivity. The coke is referred to as coke 1 and coke 2, see Fig. 8. Furthermore, the overall fit is sufficient with an SSE value of $6.659 \cdot 10^{-5}$ and an R^2 value of 0.994. However, it can be noted that the fit is overestimating the shape of the tails since the CO_2 data lacks the characteristic Gaussian tails. This discrepancy may be attributed to the data processing step, where an intensity threshold of $6 \cdot 10^{-13}$ was applied to the MS signal to remove noise, potentially suppressing the low-intensity regions of the CO_2 tails.

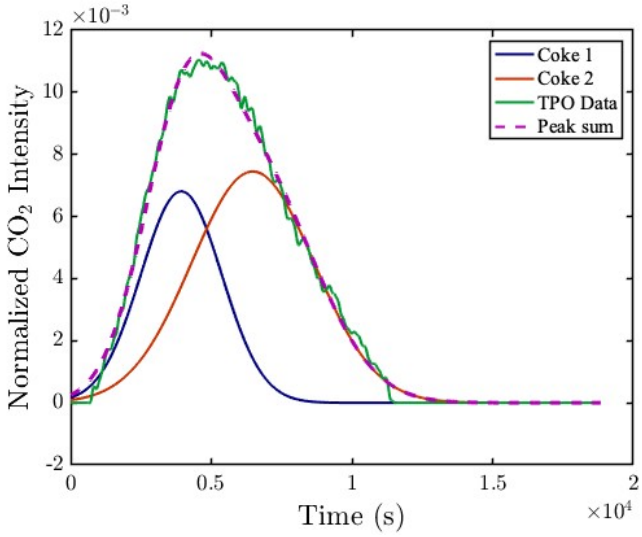

Figure 9: Deconvoluted CO_2 profile for $Pt/MgAl_2O_4$

The oxidation profile for $Pt/MgAl_2O_4$ was similarly deconvoluted, see Fig. 9. The choice to perform peak deconvolution was made due to the presence of multiple oxidation events in the TPO data, as previously explained in section 5.1.3. It can be seen in Fig. 9 that the CO_2 curve can be well approximated by two Gaussian curves. The fit gives an SSE value of $6.966 \cdot 10^{-5}$ and an R^2 of 0.996. Examining the deconvoluted peaks in more detail, it can

be seen that the oxidation profile for coke 1 is lower in magnitude and spans a narrower temperature range compared to coke 2. This result indicates that the less reactive coke is dominating, possibly corresponding to coke on the support. However, the oxidation of coke 2 does occur at an earlier temperature (and time) compared to coke 2 on Pt/Al_2O_3 (Fig. 8), indicating that the coke 2 on $Pt/MgAl_2O_4$ is more "soft" and reactive compared to coke 2 on Pt/Al_2O_3. The reactivity of each coke can further be investigated through the H/C ratio. To calculate the H/C ratio, the background-subtracted O_2 curves were also deconvoluted, see Fig. D.1-D.2 in Appendix D. The H/C ratio for each coke is presented in Table 2.

Table 2: Atomic H/C ratio of the coke deposits on each catalyst

	Pt/Al_2O_3	$Pt/MgAl_2O_4$
Coke 1	0.94	0.97
Coke 2	0.60	0.86

Examining the H/C ratios for Pt/Al_2O_3 it can be seen that coke 1 has a higher H/C ratio of 0.94, compared to coke 2 with a H/C ratio of 0.60. This is intuitive since a lower H/C ratio generally equals lower reactivity, which in turn equals oxidation at higher temperatures. Similar observations can be made for the $Pt/MgAl_2O_4$ sample, where coke 1 has a higher H/C ratio of 0.97, and coke 2 has a lower value of 0.86. Moreover, the H/C ratio for coke 1 is similar in both catalyst samples. Compounds likely to explain the coke could be alkylbenzenes or methylated biphenyl compounds which has similar H/C ratios [41]. A comparison of the H/C ratios for coke 2 suggests that coke 2 on Pt/Al_2O_3 is less reactive than that on $Pt/MgAl_2O_4$. The difference between the H/C ratios for coke 2 on the two catalysts could also be explained by the support. The $MgAl_2O_4$ support has lower acidity compared to Al_2O_3, and acid sites on the supports are often described to favor side reactions such as polymerization and dehydrogenation which can produce coke with lower H/C ratio [42][43]. Consequently, a lower H/C ratio for the Pt/Al_2O_3 catalyst supports the possibility of the coke being located on the support. Moreover, the simplest polyaromatic compound is naphthalene which has a H/C ratio of 0.8. Comparing this to the H/C ratio on $Pt/MgAl_2O_4$ it indicates that only simple polyaromatic compounds could be present in the coke. However, the lower H/C ratio for coke 2 on Pt/Al_2O_3 indicates that even larger polyaromatic compounds could be present [41]. Furthermore, it is important to note that the calculated H/C ratios are very sensitive to the choice of O_2 baseline and to the deconvoluted area. The calculated H/C ratios found in Table 2 provide an estimate of the H/C ratios of each coke family, and a more accurate determination would require further analysis. The optimal approach would involve elemental analysis, however, due to the unavailability of such an instrument, the calculated H/C ratios are deemed sufficient for modeling purposes.

5.1.5 Thermogravimetry Analysis (TGA)

TGA was performed to establish the total amount of coke on the spent catalysts. Fig. 10 displays the TGA results for Pt/Al_2O_3 and $Pt/MgAl_2O_4$ in air atmosphere over the temperature ramp. The drying phase under inert atmosphere and the isothermal step at the end are not included in the figure. The complete TGA can be found in Fig. E.1 in Appendix E.

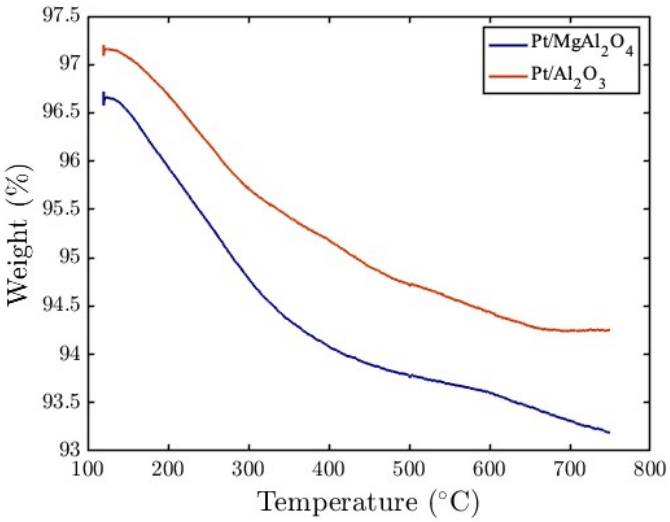

Figure 10: Thermograms of spent Pt/Al_2O_3 and $Pt/MgAl_2O_4$

From the TGA, the total weight loss was estimated to be 2.90% and 3.51% for Pt/Al_2O_3 and $Pt/MgAl_2O_4$, respectively. Comparing these values to the total carbon amount calculated from the TPO, it becomes obvious that the TG values are much lower. The TG values should, in theory, be larger than the total carbon amount derived from the TPO since the TGA measures the total mass loss, including the hydrogen in the coke. One possible explanation for the deviation is that the coke was not fully oxidized in the TGA. In the TPO the gases are passed through the catalyst bed, while in the TGA, the gases are passed from underneath the crucible, thus requiring the O_2 to diffuse into the catalyst bed. Another possible explanation could be oxidation of the Pt metal, which would increase the total weight of the sample. Furthermore, observing the TG curve for Pt/Al_2O_3 catalyst in Fig. 10, changes in the slope can be seen throughout the run until the curve appears to stabilize towards the end. On the other hand, the TG curve for $Pt/MgAl_2O_4$ displays a smooth, gradual weight loss until around 500 °C, where a change of slope can be seen, see Fig. 10. To investigate the oxidation behavior further, the DTG curves were plotted, see Fig. 11.

The peaks in the DTG (Fig. 11) correspond to the rate of mass loss, which is primarily due to coke oxidation. The peaks should therefore reflect the oxidation profile of coke, allowing comparison with the corresponding TPO oxidation profiles as displayed in Fig. 5-6. In Fig. 11a, a relatively large peak can be seen in the range 120°C - 330°C, followed by a second peak in the range 330–500 °C. These peaks correspond relatively well to the TPO profile in Fig. 5, considering that the DTG displays the loss of both carbon and hydrogen in the coke. Similarly, in Fig. 11b, a peak with a sharp rise and long tail can be seen in the range 120–500 °C, corresponding reasonably well to the TPO profile in Fig. 6. However, after 500 °C, an additional peak can be seen for both DTG curves in Fig. 11. This weight loss probably originates from dehydroxylation of the support, which has been described in literature to occur after 500 °C for alumina [44]. Furthermore, it can be seen in Fig. 11b that the DTG never reaches zero, indicating unfinished oxidation or dehydroxylation. In Fig. 11a, the DTG appears to reach zero, which indicates complete oxidation and dehydroxylation, however, it is also possible that the weight increase from Pt oxidation compensates for the decrease in weight.

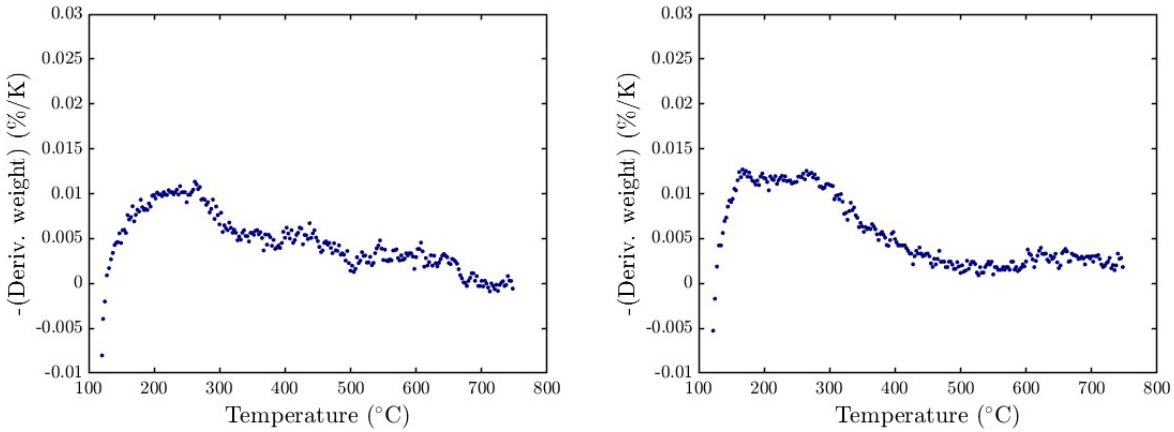

(a) Pt/Al_2O_3 (b) $Pt/MgAl_2O_4$

Figure 11: DTG curves for spent Pt/Al_2O_3 and $Pt/MgAl_2O_4$ catalysts

TGA was also performed for the same Pt catalyst samples using a heating rate of 2 °C/min, see Appendix E. The result showed a total weight loss of 3.53% and 3.29% for Pt/Al_2O_3 and $Pt/MgAl_2O_4$, respectively. The weight loss for $Pt/MgAl_2O_4$ decreased by 0.22 percentage points while the weight loss for Pt/Al_2O_3 increased by 0.63 percentage points, which indicates some degree of error in the measurements.

TGA was lastly performed on the extracted Pt/Al_2O_3 catalyst. The TGA was run twice, both samples from the same batch and with the same temperature program. The result is displayed in Fig. 12.

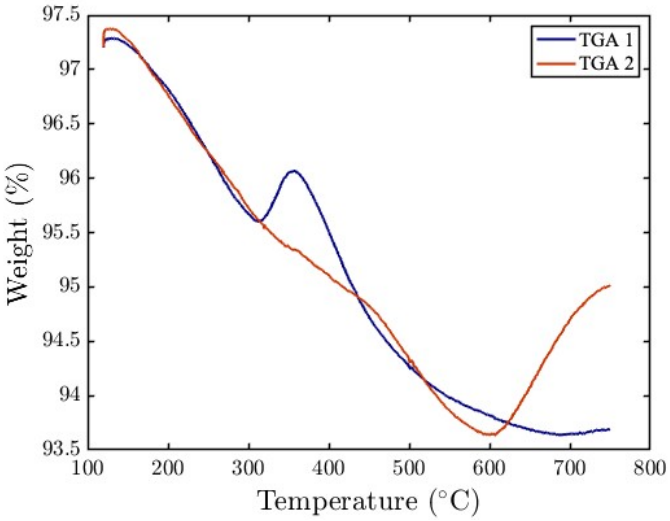

Figure 12: TGA of extracted Pt/Al_2O_3

Observing Fig. 12, it becomes obvious that the two samples exhibit different TGA profiles. Sample 1 was run first and displays a gradual loss until around 300 °C, after which a sudden 0.5% weight increase is visible. After that, the weight gradually decreases until around 700 °C, reaching a total weight loss of 3.64% at the lowest measured point. Sample 2, on the other hand, displays a gradual decrease in weight until 600°C,

where the weight is suddenly increased by around 1.4%. The total weight loss for sample 2 was measured to be 3.72% at the lowest point (∼600 °C) and 2.31% at the end of run. Both samples display unexpected results, and perhaps more importantly, differ significantly from one another. Since these samples were collected from the same batch, their decomposition behavior is expected to be identical, and the fact that they diverge so significantly points to experimental inconsistency, or artifacts in the TGA measurement. Furthermore, there is no obvious explanation for the deviation in either sample, and it becomes difficult to establish whether this is an apparent or actual mass increase. An actual mass increase would imply either metal oxidation, adsorption of species or chemical reactions producing heavier compounds. Because Pt oxidation generally occurs at elevated temperatures, it is unlikely to explain the early deviation observed in sample 1. Additionally, with only a 4 wt% Pt loading, the maximum mass gain from Pt oxidation would be too small to account for the large increase observed in sample 2. Moreover, to say with any certainty that the mass increase in either sample would be caused by adsorption or reactions involving the coke is not possible without further analysis. An apparent mass increase, on the other hand, could be the result of deviations in gas flow, which would affect the drag force of the sample scale. For instance, if the gas flow inside the TGA suddenly decreased, it is possible that the mass would appear to increase due to a reduction in the upward drag. However, a deviation in the gas flows would in all likelihood be recorded by the instrument, and no such warnings or errors were recorded for either sample. In summary, no conclusions can be drawn regarding the oxidation behavior of the extracted Pt/Al_2O_3 sample, and the TG curves displayed in Fig. 12 are deemed unreliable and thus, were not analyzed further.

5.1.6 Infrared spectroscopy (FTIR)

Several characteristic regions for carbon bonds exist. Absorption at 3000–3020 cm^{-1} is characteristic for C=C bonds in aliphatic hydrocarbons, and 3020-3200 cm^{-1} is characteristic for C=C bonds in aromatics [19]. However, no unique peaks could be found in this region, likely due to overlap with water vibrations. For instance, O-H stretch vibrations can be found in the broad region of 3650-2500 cm^{-1} [45]. The FTIR spectra for Pt/Al_2O_3 and $Pt/MgAl_2O_4$ were plotted in the region 2000–1000 cm^{-1}, see Fig. 13-14.

In Fig. 13, a small peak can be found at 1575 cm^{-1} in the coked sample that is not present in the reduced one. Bands between 1500 and 1630 cm^{-1} can represent C=C vibrations in aromatics [22]. Jianhao et al found stretch vibrations of C=C bonds in polyaromatic compounds at 1575 cm^{-1} when investigating coke deposits from propane dehydrogenation [46]. Thus, the peak at 1575 cm^{-1} may correspond to aromatic or polyaromatic compounds. This aligns with the calculated H/C ratio of 0.6 which also indicates the presence of polyaromatic compounds. Furthermore, bands between 1640–1680 cm^{-1} can be attributed to stretching vibrations of C=C bonds in alkenes [19]. However, the peak at around 1640 cm^{-1} can be found in both the coked and reduced samples (Fig. 13). This suggests that the reduced sample contains carbonaceous species or that these vibrations comes from species present in the support [45]. In addition, the extracted sample displayed the same peaks as seen for the coked sample, see Appendix F.

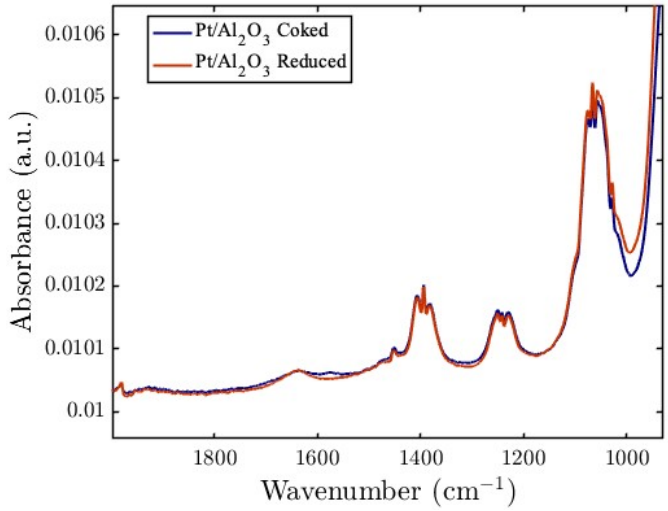

Figure 13: FTIR spectra for coked and reduced Pt/Al_2O_3 catalyst

In Fig. 14, three peaks can be found at 1407 cm^{-1}, 1494 cm^{-1} and 1640 cm^{-1}. However, none of these peaks are unique to the coked sample but are also present in the reduced sample. However, in the region 1280–1745 cm^{-1}, an increase in intensity can be seen for the coked sample. Bands between 1400 and 1450 cm^{-1} can correspond to vibrations in branched aliphatics, and bands between 1350-1470 cm^{-1} can reflect bending vibrations of C-H in the CH_3 (methyl) and CH_2 (methylene) groups [19] [22]. In addition, bands between 1640–1680 cm^{-1} usually represent stretching vibrations of C=C in alkenes, and 1500–1630 cm^{-1} can represent vibrations in aromatics [22][19]. However, because the same bands appear in both the coked and the reduced spectra, the bands may arise from non-coke species such as adsorbed water or the support. Proper evaluation of the nature of coke would require further analysis of the reduced sample and potentially additional analysis using e.g. Raman. In summary, the peak at 1575 cm^{-1} could correspond to vibrations in aromatic or polyaromatic compounds in the Pt/Al_2O_3 sample, but to obtain more detailed information about the nature of coke, additional analysis would be required.

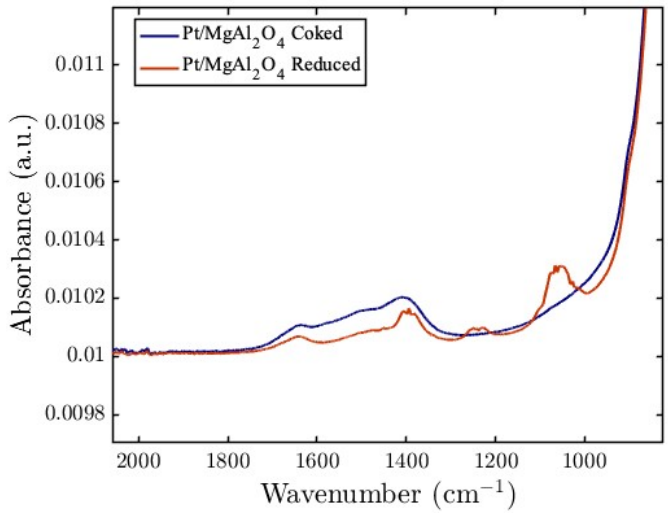

Figure 14: FTIR spectra for coked and reduced $Pt/MgAl_2O_4$ catalyst

5.2 Modeling

5.2.1 Criteria Evaluation

The assumption of negligible dispersion was verified with tracer tests, in which a step injection of O_2 was performed through the reactor (glass wool and bed) and only the glass wool. In Fig. 15a, the response curves for the tracer through the reactor and glass wool can be seen along with the fitted cumulative function, F(t). The step response displays a slight tilt in the slope for both curves, indicating some degree of dispersion in the system. The dispersion could originate from several sources, such as the glass wool, bed, or tubing and valves. The residence time distribution functions (RDT) were also plotted, see Fig. 15b.

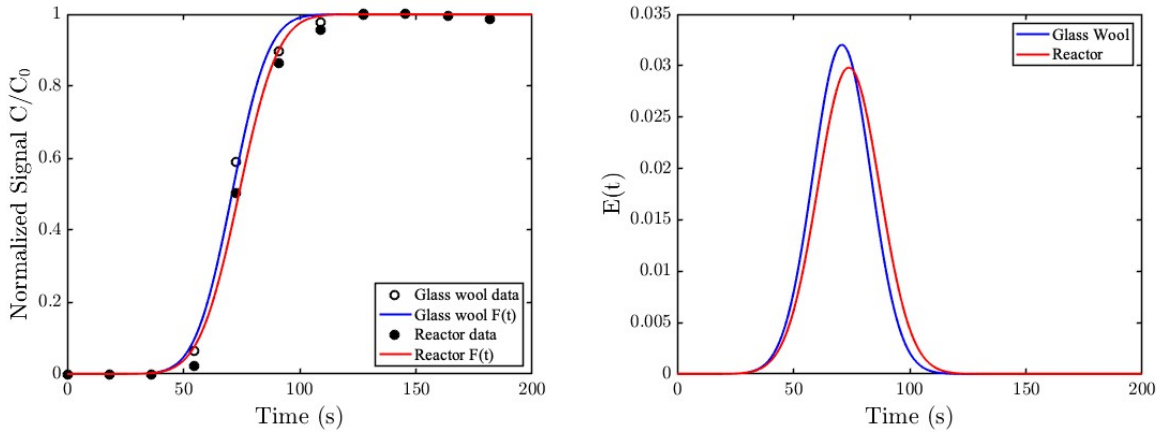

(a) (b)

Figure 15: Tracer tests results displaying (a) the cumulative residence time distribution, F(t), and (b) the residence time distribution, E(t)

In Fig. 15b, it can be seen that the residence time and standard deviation are slightly lower for the glass wool, indicating lesser dispersion than the reactor. A complete overlap would indicate no dispersion in the bed, however, the difference between the curves is negligible (within experimental error), suggesting minimal dispersion in the bed. The Péclet number was calculated to be 60.33 and 61.51 for the reactor and glass wool, respectively. This further indicates that the dispersion contribution from the bed is small and thus dispersion is considered negligible. Furthermore, the Weisz-Prater and Mears criteria were calculated for each catalyst and coke family, see Table 3-4. All values for WP and MR fulfill the criteria of WP $\ll 1$ and MR < 0.15.

Table 3: Weisz Prater and Mears criteria for Pt/Al_2O_3

Coke family	**WP**	**MR**
Coke 1	$2.36{\cdot}10^{-5}$	$6.20{\cdot}10^{-3}$
Coke 2	$6.66{\cdot}10^{-6}$	$9.00{\cdot}10^{-4}$

Table 4: Weisz Prater and Mears criteria for $Pt/MgAl_2O_4$

Coke family	**WP**	**MR**
Coke 1	$1.37 \cdot 10^{-5}$	$1.80 \cdot 10^{-3}$
Coke 2	$1.39 \cdot 10^{-5}$	$1.90 \cdot 10^{-5}$

5.2.2 Model Fit and Parameter Estimation

A comparison between the model fit and experimental CO_2 evolution for Pt/Al_2O_4 is provided in Fig. 16.

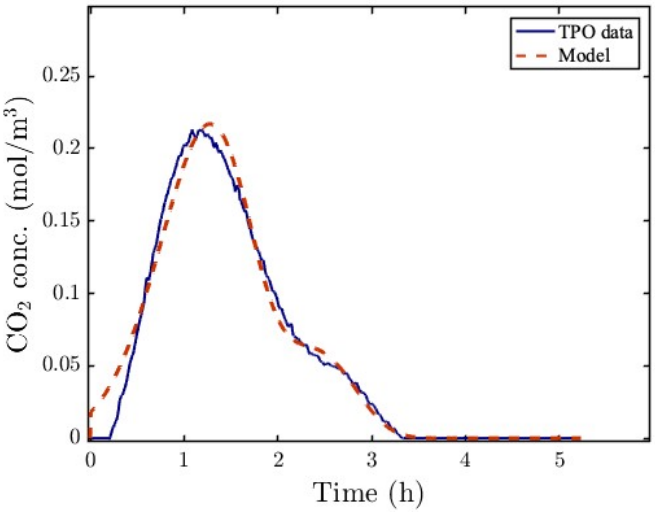

Figure 16: Model fit for Pt/Al_2O_3

It can be seen in Fig. 16 that the model is capable of capturing the overall shape and magnitude of the CO_2 evolution, including the shoulder peak. The largest discrepancy can be observed at the beginning of the CO_2 evolution, where the model appears to overestimate the CO_2 formation. There is no obvious explanation for the deviation between the model and experimental data, and to fully assess the models ability to predict the oxidation of coke, model verification using independent experimental data would be necessary. In addition, it would be beneficial to perform experiments with a lower heating rate to potentially capture more details in the oxidation behavior. However, due to limited amounts of catalyst samples and the time constraints of this project, neither has been performed. Potential explanations for the discrepancy could be that the assumption of negligible dispersion or ideal behavior is wrong. There could also be errors in the data processing step or estimation of initial conditions. Nevertheless, the model can predict the general oxidation behavior of the coke with satisfactory accuracy, and the estimated kinetic parameters are presented in Table 5.

Table 5: Estimated kinetic parameters for oxidation of each coke family on Pt/Al_2O_3 with 95% confidence

Coke family	**Ea (kJ/mol)**	$\mathbf{k}_{ref}$ **(m^3/mol · s)**
Coke 1	46.54 ± 0.50	$3.58{\cdot}10^{-4} \pm 5.2{\cdot}10^{-6}$ *
Coke 2	68.78 ± 2.47	$3.83{\cdot}10^{-4} \pm 1.8{\cdot}10^{-5}$ **

* *At reference temperature 546.1 K*
** *At reference temperature 674.5 K*

The estimated parameters in Table 5 show that coke 1 oxidizes at lower temperatures, with a lower activation energy and a relatively high rate constant at 546.1 K. This is consistent with a more reactive, hydrogen-rich coke species likely deposited on or near the platinum metal sites. In contrast, coke 2 exhibits a higher activation energy and a similar rate constant at a higher reference temperature (674.5 K), consistent with more dehydrogenated coke, possibly located on the support. Moreover, the correlation matrix is shown in Table 6. The correlation values between Ea and k_{ref} for each coke suggest that the estimated parameters are moderately correlated, but not strongly, which supports their credibility. In addition, a low correlation between the kinetic parameters of the different coke families can be observed. Reduction in parameter correlation can be performed through optimization of the reference temperatures [37]. However, such optimization was not performed in this study.

Table 6: Correlation matrix of fitted kinetic parameters for each coke family on Pt/Al_2O_3

	$k_{ref,1}$	$k_{ref,2}$	Ea_1	Ea_2
$k_{ref,1}$	1	0.39	0.53	0.27
$k_{ref,2}$	0.39	1	0.16	0.46
Ea_1	0.53	0.16	1	0.38
Ea_2	0.27	0.46	0.38	1

Furthermore, the model fit and experimental CO_2 data for coke oxidation on $Pt/MgAl_2O_4$ are shown in Fig. 17. The model captures the general behavior of the experimental data, but overestimates the CO_2 production at lower temperatures, similar to that observed for Pt/Al_2O_4 (Fig. 16). The fit also displays a slightly oscillating behavior over the TPO data, pending between over- and underestimations. The estimated kinetic parameters can be found in Table 7

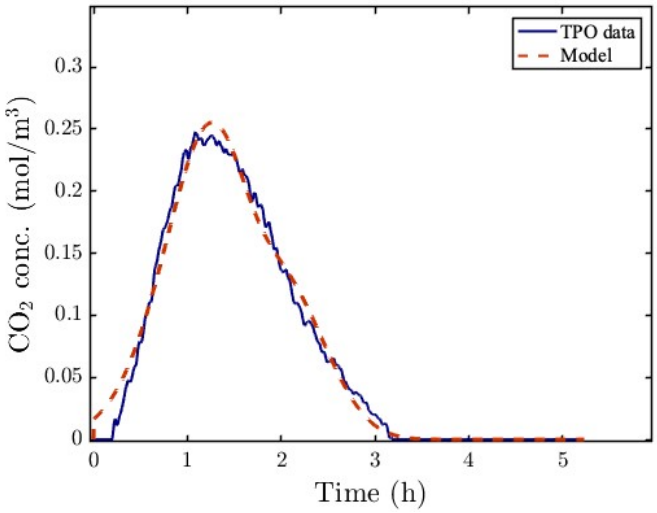

Figure 17: Model fit for $Pt/MgAl_2O_4$

Table 7: Estimated kinetic parameters for oxidation of each coke family on $Pt/MgAl_2O_4$ with 95% confidence

Coke family	**Ea (kJ/mol)**	**k$_{ref}$ (m^3/mol · s)**
Coke 1	53.68 ± 0.79	$3.27{\cdot}10^{-4} \pm 8.3{\cdot}10^{-6}$ *
Coke 2	43.52 ± 0.78	$2.17{\cdot}10^{-4} \pm 3.4{\cdot}10^{-6}$ **

* *At reference temperature 522.4 K*
** *At reference temperature 594.7 K*

Interestingly, the kinetic parameters in Table 7 show a higher activation energy for coke 1 compared to coke 2. However, observing the reaction rate coefficient, it can be seen that the reaction rate is higher for coke 1 at a lower temperature than coke 2, suggesting a lower reaction rate for coke 2. The reaction rate coefficient depends on both activation energy and the pre-exponential factor. And thus, a low activation energy does not simply imply a faster reaction. Furthermore, observing the correlation matrix in Table 8, it can be noted that the correlation between Ea and k_{ref} for each coke is relatively low. However, it can also be seen that the correlation between the rate coefficient for coke 1, $k_{ref,1}$, and the activation energy for coke 2, Ea_2, is relatively high with a value of 0.72. The reason for this high correlation is not obvious, but it is likely caused by the overlap between the oxidation events. When one peak shifts, it is possible that the optimizer compensates by adjusting the other, so their fitted parameters move together even though they describe different reactions. The activation energy for coke 2 can be compared to the literature to investigate the credibility of the estimated value. For instance, Shakor et al reported an activation energy of 41.53 kJ/mol for soft-coke oxidation on spent hydrocracking/reforming catalysts [47]. The estimated values, therefore, fall within literature-credible ranges but should be verified with additional experiments.

Moreover, during the modeling, several local minima could be found, giving somewhat good model fits with relatively low residuals, but with different kinetic parameters. For instance, one solution predicted that coke 2 oxidizes faster than coke 1, suggesting that the

Table 8: Correlation matrix of fitted kinetic parameters for each coke family on $Pt/MgAl_2O_4$

	$k_{ref,1}$	$k_{ref,2}$	Ea_1	Ea_2
$k_{ref,1}$	1	0.26	0.37	0.72
$k_{ref,2}$	0.26	1	-0.16	0.42
Ea_1	0.37	-0.16	1	0.15
Ea_2	0.72	0.42	0.15	1

two species had exchanged positions in the TPO profile. This is also likely a result of the overlapping oxidation profiles rather than the model itself. The presence of overlapping oxidation events may allow multiple sets of parameters to adequately describe the TPO profile as previously discussed. Performing TPO with a lower heating rate could once again be beneficial to capture more details in the oxidation behavior and potentially separate the peaks further. Additionally, verifying the obtained kinetic parameters using additional TPO experiments would be beneficial, but was not performed due to time constraints.

5.2.3 Regeneration

The model was solved for constant temperature and flow, considering the estimated kinetic parameters presented in section 5.2.2. The regeneration or coke oxidation was plotted over time, see Fig. 18.

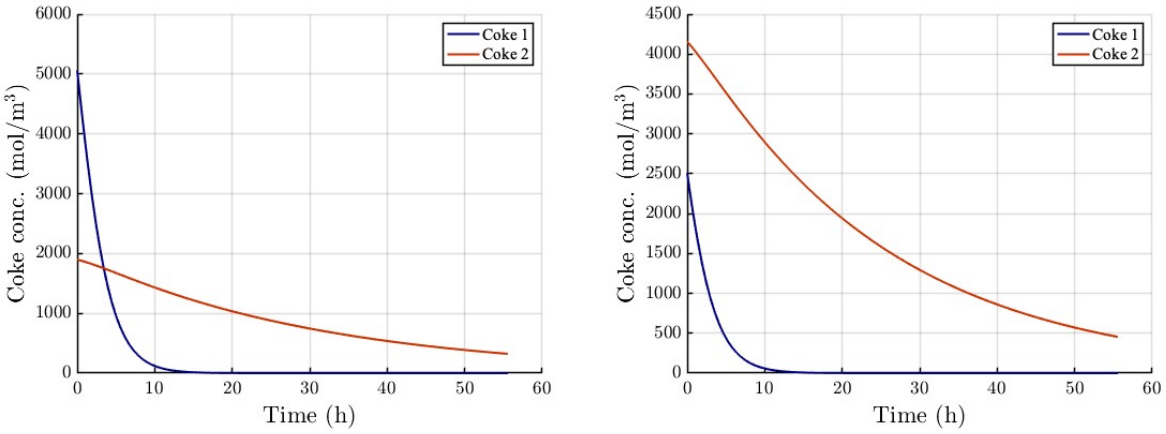

Figure 18: Regeneration at 300 °C in 1 % O_2 of coked (a) Pt/Al_2O_3 and (b) $Pt/MgAl_2O_4$

The profiles in Fig. 18 reflect the reactivity of the two coke families on each catalyst. It can be observed that coke 1 oxidizes much faster on both catalysts, and that coke 2 is more persistent. Because the $Pt/MgAl_2O_4$ sample has been on stream for roughly four times longer than Pt/Al_2O_3, it started the regeneration with a larger coke 2 amount. For this reason, the coke 2 consumption rate is higher in the beginning on the $Pt/MgAl_2O_4$ catalysts. Despite this, both catalysts converge to a similar coke 2 concentration after 55 h. Furthermore, to provide a comparison on the catalyst regeneration, the two catalysts

were simulated using their estimated parameters and the properties of $Pt/MgAl_2O_4$ (bed length, density, concentration ect.). The regeneration was simulated at 300 °C and 280 °C in 1% O_2, see Fig. 19a-19b.

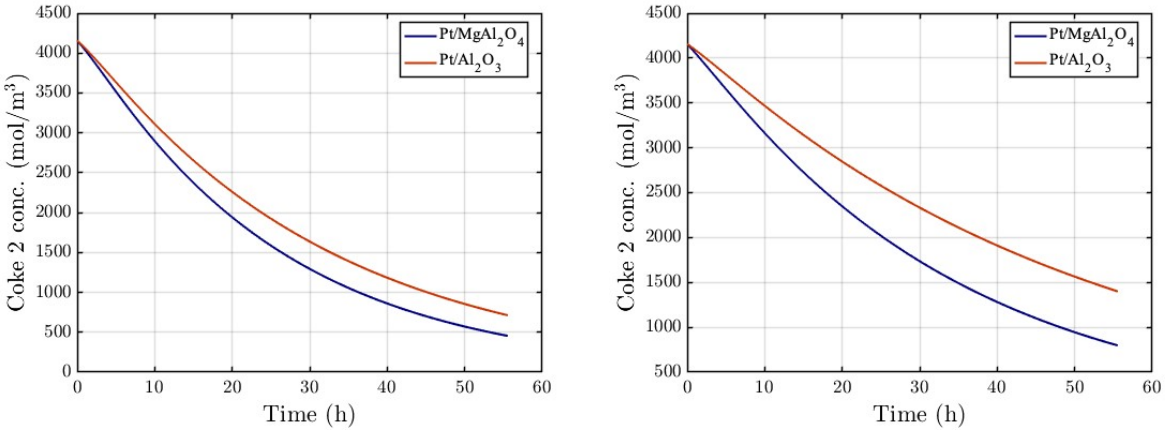

Figure 19: Regeneration using 1%O_2 at (a) 300 °C and (b) 280°C

In Fig. 19, it can be seen that coke 2 burns off faster on $Pt/MgAl_2O_4$ than on Pt/Al_2O_3 for both temperatures. It can also be observed that decreasing the temperature decreases how much coke is oxidized for both catalysts. However, it can be seen that coke 2 on $Pt/MgAl_2O_4$ is less affected by the lower temperature, likely due to the low activation energy as seen in Table 7. Observing the figures, it can even be noted that the final concentration of coke on $Pt/MgAl_2O_4$ after 55 h at 280 °C is very similar to that for Pt/Al_2O_4 at 300 °C. In summary, due to the higher reactivity of coke 2 on $Pt/MgAl_2O_4$ it oxidizes faster, thus giving faster regeneration and better performance at lower temperatures. If coke 2 corresponds to coke on the support, this would imply that the $MgAl_2O_4$ support influences how much coke forms and how readily that coke can be removed during regeneration. Performing further experiments, testing different metal loading and TOS might provide further information on the effect of the different supports on the coke formation. Furthermore, it is important to consider the high TOS for both catalysts. In a real industrial process, a catalyst would not be deactivated to the same extent as performed in this work. Lower TOS would affect both the amount of coke and the degree of dehydrogenation and reactivity. Therefore, the total time for regeneration displayed in Fig. 18 might not be representative of a real system. In addition, modeling the regeneration considering both mass transport limitations (with varying particle sizes) and a non-isothermal operation would be required to better simulate a real system.

The operating conditions in Fig. 18-19 were chosen arbitrarily to provide a comparison of the regeneration between the catalysts. However, the selection of temperature and O_2 concentration is crucial for efficient and safe regeneration. Therefore, the model was solved with varying temperatures and O_2 concentrations, and the coke 2 oxidation was plotted for $Pt/MgAl_2O_4$, see Fig. 20.
In Fig. 20 it can be seen that both increasing the temperature and the concentration result in faster regeneration. However, the best choice of regeneration conditions would not simply be to select the highest temperature and O_2 concentration. Increasing the temperature and O_2 would decrease the time of regeneration but also result in faster heat

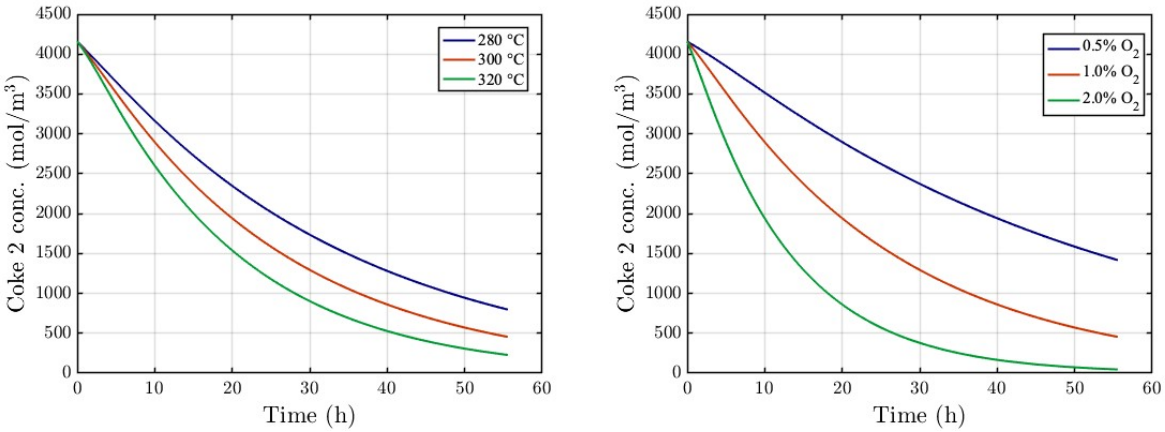

(a) (b)

Figure 20: Regeneration of $Pt/MgAl_2O_4$ varying (a) temperature with constant concentration, 1%O_2, and (b) concentration with constant temperature, 300°C

generation, potentially damaging the reactor and catalyst. Too high temperature can lead to catalyst decay through, for instance, sintering, which permanently damages the catalyst [16]. To avoid high temperature waves but still achieve faster regeneration time, it is possible to begin at low O_2 concentrations and gradually increase the O_2 concentration [16]. Then the reaction and heat formation remain limited at the beginning of the regeneration, where most of the coke is oxidized, and the reaction rate is increased at the end of regeneration, where small amounts of coke remain. However, to properly asses the optimal temperature and O_2 concentration for the coked $Pt/MgAl_2O_4$ and the Pt/Al_2O_3 catalysts, expanding the model to include transport limitations and heat generation would be required.

6. Conclusions & Future prospects

Both the active metal and the support affect the coke formation in the dehydrogenation of MCH. The Pt-based catalysts showed higher activity with a higher degree of coking compared to the Ni-based catalysts, and the $Pt/MgAl_2O_4$ catalyst displayed the highest coking resistance with the longest TOS.

From the TPO experiments, two oxidation regions, possibly corresponding to coke on the metal and support, could be distinguished on the coked Pt/Al_2O_4 and $Pt/MgAl_2O_4$ catalysts. Coke 2, which is presumably located on the support, was found to have an H/C ratio of 0.86 on the $Pt/MgAl_2O_4$ and 0.6 on Pt/Al_2O_3. The lower H/C ratio on Pt/Al_2O_3 indicates more dehydrogenated and polyaromatic coke despite the shorter TOS, which can be attributed to the higher acidity of the Al_2O_3 support.

Furthermore, the TGA displayed poor reproducibility and reported a lower total coke amount than the TPO, likely because of incomplete coke oxidation or overlapping events, such as metal oxidation. The DTG curves were noisy and exhibited a slight mass loss, most likely from support dehydroxylation, making the method less reliable than TPO for analyzing oxidation behavior. Soxhlet extraction tests to remove soluble coke were inconclusive since the TPO of the extracted sample failed, while the GC-MS analysis provided limited information. Nevertheless, GC-MS analysis of the extract indicated the presence of biphenyl structures which is in line with the postulation of polyaromatic coke formation on the Al_2O_3 support. Moreover, FTIR analysis of the coked Pt/Al_2O_3 catalyst indicated the presence of a peak at 1575 cm^{-1}, possibly representing vibrations in polyaromatic compounds for the Pt/Al_2O_3. In contrast, FTIR of the coked $Pt/MgAl_2O_4$ did not exhibit any additional peaks, but rather increased intensity in peaks, corresponding to aliphatic and aromatic compounds.

The kinetic model proved successful in estimating realistic kinetic parameters that capture the coke oxidation behavior on the Pt/Al_2O_4 and $Pt/MgAl_2O_4$ catalysts. The activation energies were estimated to be 46.54 kJ/mol and 68.78 kJ/mol for the two coke families found on Pt/Al_2O_3 and estimated to be 53.68 kJ/mol and 43.52 kJ/mol for the two coke families found on $Pt/MgAl_2O_4$. However, model validation with external experiments would be required to verify the credibility of the parameters. Additionally, simulation of the regeneration process showed that coke 2 was less reactive and thus more difficult to remove through oxidation on both catalysts, compared to coke 1. However, coke 2 was more reactive and thus easier to oxidize on the $MgAl_2O_4$ support than on Al_2O_3 further indicating that lower acidity of the support is beneficial to reduce the formation of more dehydrogenated or "hard" coke.

In this thesis, the regeneration process was modeled under isothermal conditions and without consideration of mass transport limitations. To further study the regeneration and formation of heat waves, it would be of interest to construct a more comprehensive regeneration model describing both mass transport limitations (varying particle size) and the effects of heat generation under non-isothermal conditions. The modeling of heat

waves is essential for the potential scale-up of the system. Moreover, to gain further understanding of the coke oxidation behavior on Pt/Al_2O_3 and $Pt/MgAl_2O_4$ catalysts, it would be of interest to study the catalysts using different metal loadings and under different TOS. Using analytical tools such as Raman and elemental analysis could provide a deeper understanding of the nature of the coke and is thus recommended for future work.

Bibliography

[1] International Energy Agency, "Net Zero by 2050 - A Roadmap for the Global Energy Sector," en, IEA, Tech. Rep., 2021.

[2] *Energy storage*, en. [Online]. Available: https://energy.ec.europa.eu/topics/research-and-technology/energy-storage_en (visited on 02/11/2025).

[3] D. Acharya, D. Ng, and Z. Xie, "Recent Advances in Catalysts and Membranes for MCH Dehydrogenation: A Mini Review," *Membranes (Basel)*, vol. 11, no. 12, p. 955, 2021, Place: Switzerland Publisher: MDPI AG, ISSN: 2077-0375. DOI: 10.3390/membranes11120955.

[4] H. S. Alghamdi, A. Ali, A. M. Ajeebi, *et al.*, "Catalysts for Liquid Organic Hydrogen Carriers (LOHCs): Efficient Storage and Transport for Renewable Energy," *Chemical record*, vol. 24, no. 11, e202400082–n/a, 2024, Place: United States Publisher: Wiley Subscription Services, Inc, ISSN: 1527-8999. DOI: 10.1002/tcr.202400082.

[5] J. Jangir and B. R. Jagirdar, "Unveiling the Potential of Heterogeneous Systems for Reversible Hydrogen Storage in Liquid Organic Hydrogen Carriers," *ChemSusChem*, e202402018, 2024, Place: Germany, ISSN: 1864-5631. DOI: 10.1002/cssc.202402018.

[6] M. D. P. Sørensen, "The establishment of a coke-burn kinetic model for zeolite catalysts," *Chemical engineering science*, vol. 168, pp. 465–479, 2017, Publisher: Elsevier Ltd, ISSN: 0009-2509. DOI: 10.1016/j.ces.2017.05.014.

[7] X. Dai, R. Verma, X. Zhang, *et al.*, "Critical analysis on catalytic methylcyclohexane dehydrogenation reaction: A review," *International journal of hydrogen energy*, 2024, Publisher: Elsevier Ltd, ISSN: 0360-3199. DOI: 10.1016/j.ijhydene.2024.08.148.

[8] J. Gao, N. Li, D. Zhang, S. Zhao, and Y. Zhao, "The progress of research based on methylcyclohexane dehydrogenation technology: A review," *International journal of hydrogen energy*, vol. 85, pp. 865–880, 2024, Publisher: Elsevier Ltd, ISSN: 0360-3199. DOI: 10.1016/j.ijhydene.2024.08.331.

[9] H. Wang, B. Wang, H. Kong, X. Lu, and X. Hu, "Thermodynamic Analysis of Methylcyclohexane Dehydrogenation and Solar Energy Storage via Solar-Driven Hydrogen Permeation Membrane Reactor," *Membranes (Basel)*, vol. 10, no. 12, p. 374, 2020, Place: Switzerland Publisher: MDPI AG, ISSN: 2077-0375. DOI: 10.3390/membranes10120374.

[10] S. Yolcular and Ö. Olgun, "Ni/Al2O3 catalysts and their activity in dehydrogenation of methylcyclohexane for hydrogen production," *Selected papers from the EUROPACAT VIII Hydrogen Society Session, Turku, Finland, 26-31 August 2007*, vol. 138, no. 3, pp. 198–202, Nov. 2008, ISSN: 0920-5861. DOI: 10.1016/j.cattod.2008.07.020. [Online]. Available: https://www.sciencedirect.com/science/article/pii/S0920586108003556.

[11] Y. Sekine and T. Higo, "Recent Trends on the Dehydrogenation Catalysis of Liquid Organic Hydrogen Carrier (LOHC): A Review," *Topics in Catalysis*, vol. 64, no. 7, pp. 470–480, Jul. 2021, ISSN: 1572-9028. DOI: 10.1007/s11244-021-01452-x. [Online]. Available: https://doi.org/10.1007/s11244-021-01452-x.

[12] A. H. Al-ShaikhAli, A. Jedidi, L. Cavallo, and K. Takanabe, "Non-precious bimetallic catalysts for selective dehydrogenation of an organic chemical hydride system," *Chemical communications (Cambridge, England)*, vol. 51, no. 65, pp. 12 931–12 934, 2015, Place: England, ISSN: 1359-7345. DOI: 10.1039/C5CC04016G.

[13] F. Alhumaidan, D. Tsakiris, D. Cresswell, and A. Garforth, "Hydrogen storage in liquid organic hydride: Selectivity of MCH dehydrogenation over monometallic and bimetallic Pt catalysts," *International journal of hydrogen energy*, vol. 38, no. 32, pp. 14 010–14 026, 2013, Place: OXFORD Publisher: Elsevier Ltd, ISSN: 0360-3199. DOI: 10.1016/j.ijhydene.2013.08.067.

[14] C. H. Bartholomew and R. J. Farrauto, *Fundamentals of industrial catalytic processes*, 2. ed. Hoboken, N.J: Wiley, 2006, ISBN: 0-471-45713-2.

[15] S. K. Sahoo, P. Rao, D. Rajeshwer, K. R. Krishnamurthy, and I. D. Singh, "Structural characterization of coke deposits on industrial spent paraffin dehydrogenation catalysts," *Applied catalysis. A, General*, vol. 244, no. 2, pp. 311–321, 2003, Place: Amsterdam Publisher: Elsevier B.V, ISSN: 0926-860X. DOI: 10.1016/S0926-860X(02)00603-8.

[16] M. D. Argyle and C. H. Bartholomew, "Heterogeneous Catalyst Deactivation and Regeneration: A Review," *Catalysts*, vol. 5, no. 1, pp. 145–269, 2015, Place: Basel Publisher: MDPI AG, ISSN: 2073-4344. DOI: 10.3390/catal5010145.

[17] M. Baerns, *Basic Principles in Applied Catalysis* (Springer Series in Chemical Physics, 75), 1st ed. 2004. Berlin, Heidelberg: Springer Berlin Heidelberg, 2004, ISBN: 3-662-05981-9. DOI: 10.1007/978-3-662-05981-4.

[18] S. He, C. Sun, X. Yang, B. Wang, X. Dai, and Z. Bai, "Characterization of coke deposited on spent catalysts for long-chain-paraffin dehydrogenation," *Chemical engineering journal (Lausanne, Switzerland : 1996)*, vol. 163, no. 3, pp. 389–394, 2010, Place: Oxford Publisher: Elsevier B.V, ISSN: 1385-8947. DOI: 10.1016/j.cej.2010.07.024.

[19] Q. Li, Z. Sui, X. Zhou, Y. Zhu, J. Zhou, and D. Chen, "Coke Formation on Pt–Sn/Al2O3 Catalyst in Propane Dehydrogenation: Coke Characterization and Kinetic Study," *Topics in catalysis*, vol. 54, no. 13-15, pp. 888–896, 2011, Place: Boston Publisher: Springer US, ISSN: 1022-5528. DOI: 10.1007/s11244-011-9708-8.

[20] M. Santhosh Kumar, D. Chen, A. Holmen, and J. C. Walmsley, "Dehydrogenation of propane over Pt-SBA-15 and Pt-Sn-SBA-15: Effect of Sn on the dispersion of Pt and catalytic behavior," *Selection of papers presented in Session 10, Natural Gas Conversion, at the Europacat VIII Conference, Turku (Åbo), Finland, August 26-31, 2007*, vol. 142, no. 1, pp. 17–23, Apr. 2009, ISSN: 0920-5861. DOI: 10.1016/j.cattod.2009.01.002. [Online]. Available: https://www.sciencedirect.com/science/article/pii/S0920586109000236.

[21] J. Zhou, J. Zhao, J. Zhang, T. Zhang, M. Ye, and Z. Liu, "Regeneration of catalysts deactivated by coke deposition: A review," *Chinese Journal of Catalysis*, vol. 41, no. 7, pp. 1048–1061, Jul. 2020, ISSN: 1872-2067. DOI: 10.1016/S1872-2067(20)63552-5. [Online]. Available: https://www.sciencedirect.com/science/article/pii/S1872206720635525.

[22] H.-Z. Wang, L.-L. Sun, Z.-J. Sui, *et al.*, "Coke Formation on Pt–Sn/Al2O3 Catalyst for Propane Dehydrogenation," *Industrial & engineering chemistry research*, vol. 57, no. 26, pp. 8647–8654, 2018, Publisher: American Chemical Society, ISSN: 0888-5885. DOI: 10.1021/acs.iecr.8b01313.

[23] J. P. Ruelas-Leyva, L. F. Maldonado-Garcia, A. Talavera-Lopez, *et al.*, "A Comprehensive Study of Coke Deposits on a Pt-Sn/SBA-16 Catalyst during the Dehydrogenation of Propane," *Catalysts*, vol. 11, no. 1, p. 128, 2021, Place: Basel Publisher: MDPI AG, ISSN: 2073-4344. DOI: 10.3390/catal11010128.

[24] Y. Wu, Y. Li, X. Yu, *et al.*, "Insights into size effects of Pt/Al2O3 catalysts on hydrogen production from methylcyclohexane dehydrogenation," *Catalysis science & technology*, vol. 14, no. 7, pp. 1791–1801, 2023, Place: Cambridge Publisher: Royal Society of Chemistry, ISSN: 2044-4753. DOI: 10.1039/d3cy01568h.

[25] J. C. Afonso, M. Schmal, and R. Fréty, "The chemistry of coke deposits formed on a Pt Sn catalyst during dehydrogenation of n-alkanes to mono-olefins," *Fuel processing technology*, vol. 41, no. 1, pp. 13–25, 1994, Place: Amsterdam Publisher: Elsevier B.V, ISSN: 0378-3820. DOI: 10.1016/0378-3820(94)90056-6.

[26] L. Wang and C. L. Weller, "Recent advances in extraction of nutraceuticals from plants," *Trends in Food Science & Technology*, vol. 17, no. 6, pp. 300–312, Jun. 2006, ISSN: 0924-2244. DOI: 10.1016/j.tifs.2005.12.004. [Online]. Available: https://www.sciencedirect.com/science/article/pii/S0924224405003559.

[27] J. Van Doorn and J. Moulijn, "Extraction of spent hydrotreating catalysts studied by fourier transform infra-red spectroscopy," *Fuel processing technology*, vol. 26, no. 1, pp. 39–51, 1990, Publisher: Elsevier B.V, ISSN: 0378-3820. DOI: 10.1016/0378-3820(90)90022-K.

[28] M. Schwaab and J. C. Pinto, "Optimum reference temperature for reparameterization of the Arrhenius equation. Part 1: Problems involving one kinetic constant," *Chemical engineering science*, vol. 62, no. 10, pp. 2750–2764, 2007, Place: Oxford Publisher: Elsevier Ltd, ISSN: 0009-2509. DOI: 10.1016/j.ces.2007.02.020.

[29] C. Perego and S. Peratello, "Experimental methods in catalytic kinetics," *Catalysis today*, vol. 52, no. 2, pp. 133–145, 1999, Place: Amsterdam Publisher: Elsevier B.V, ISSN: 0920-5861. DOI: 10.1016/S0920-5861(99)00071-1.

[30] H. S. Fogler, B. R. Goldsmith, E. Nikolla, and N. Singh, *Elements of chemical reaction engineering* (International series in the physical and chemical engineering sciences), 7th edition. Place of publication not identified: Pearson, 2024, ISBN: 978-0-13-533756-1.

[31] G. F. Froment, K. B. Bischoff, and J. De Wilde, *Chemical reactor analysis and design*, en, 3. ed. Hoboken, NJ: Wiley, 2011, ISBN: 978-0-470-56541-4.

[32] L. Edsberg, *Introduction to computation and modeling for differential equations*, Second edition. Chichester, West Sussex: Wiley Blackwell, 2016, ISBN: 978-1-119-01844-5.

[33] W. E. Schiesser and G. W. Griffiths, "An Introduction to the Method of Lines," in United States: Cambridge University Press, 2009, pp. 1–17, ISBN: 0-521-51986-1. DOI: 10.1017/CBO9780511576270.002.

[34] K. Postawa, J. Szczygieł, and M. Kułażyński, "A comprehensive comparison of ODE solvers for biochemical problems," *Renewable Energy*, vol. 156, pp. 624–633, Aug. 2020, ISSN: 0960-1481. DOI: 10.1016/j.renene.2020.04.089. [Online]. Available: https://www.sciencedirect.com/science/article/pii/S0960148120306212.

[35] L. F. Shampine and M. W. Reichelt, "The MATLAB ODE Suite," *SIAM Journal on Scientific Computing*, vol. 18, no. 1, pp. 1–22, Jan. 1997, Publisher: Society for Industrial and Applied Mathematics, ISSN: 1064-8275. DOI: 10.1137/S1064827594276424. [Online]. Available: https://doi.org/10.1137/S1064827594276424 (visited on 06/16/2025).

[36] S. Sun and J. Nocedal, "A Trust Region Method for the Optimization of Noisy Functions," 2022. DOI: 10.48550/arxiv.2201.00973.

[37] M. Schwaab, L. P. Lemos, and J. C. Pinto, "Optimum reference temperature for reparameterization of the Arrhenius equation. Part 2: Problems involving multiple reparameterizations," *Chemical engineering science*, vol. 63, no. 11, pp. 2895–2906, 2008, Place: Oxford Publisher: Elsevier Ltd, ISSN: 0009-2509. DOI: 10.1016/j.ces.2008.03.010.

[38] N. O. o. D. a. Informatics, *Carbon dioxide*, en, Publisher: National Institute of Standards and Technology. [Online]. Available: https://webbook.nist.gov/cgi/cbook.cgi?ID=C124389&Mask=200 (visited on 06/01/2025).

[39] M. A. van Spronsen, J. W. M. Frenken, and I. M. N. Groot, "Surface science under reaction conditions: CO oxidation on Pt and Pd model catalysts," *Chemical Society reviews*, vol. 46, no. 14, pp. 4347–4374, 2017, Place: England, ISSN: 0306-0012. DOI: 10.1039/c7cs00045f.

[40] S. Dey and N. Mehta, "Oxidation of carbon monoxide over various nickel oxide catalysts in different conditions: A review," *Chemical Engineering Journal Advances*, vol. 1, p. 100 008, Sep. 2020, ISSN: 2666-8211. DOI: 10.1016/j.ceja.2020.100008. [Online]. Available: https://www.sciencedirect.com/science/article/pii/S2666821120300089.

[41] E. T. Vogt, D. Fu, and B. M. Weckhuysen, "Carbon Deposit Analysis in Catalyst Deactivation, Regeneration, and Rejuvenation," 2023, ISSN: 1433-7851.

[42] Z. Lian, C. Si, F. Jan, S. Zhi, and B. Li, "Coke Deposition on Pt-Based Catalysts in Propane Direct Dehydrogenation: Kinetics, Suppression, and Elimination," *ACS catalysis*, vol. 11, no. 15, pp. 9279–9292, 2021, Publisher: American Chemical Society, ISSN: 2155-5435. DOI: 10.1021/acscatal.1c00331.

[43] H. Zhang, F. Feng, F. Meng, *et al.*, "Optimizing propylene selectivity and stability over Pt–Sn/MgAl2O4 catalysts for propane dehydrogenation," *Journal of porous materials*, vol. 31, no. 4, pp. 1257–1267, 2024, Place: New York Publisher: Springer US, ISSN: 1380-2224. DOI: 10.1007/s10934-024-01578-9.

[44] M. L. Rahman, M. S. Islam, M. F. Ahmed, B. Biswas, N. Sharmin, and A. J. M. T. Neger, "Extraction and characterization of highly pure alumina (, , and) polymorphs from waste beverage cans: A viable waste management approach," *Arabian Journal of Chemistry*, vol. 16, no. 2, p. 104 518, Feb. 2023, ISSN: 1878-5352. DOI: 10.1016/j.arabjc.2022.104518. [Online]. Available: https://www.sciencedirect.com/science/article/pii/S1878535222008346.

[45] N. L. Alpert, W. E. Keiser, and H. A. Szymanski, *IR : theory and practice of infrared spectroscopy*, Second edition. New York, New York: Plenum Press, 1970, ISBN: 1-4684-8160-6. DOI: 10.1007/978-1-4684-8160-0.

[46] Jianhao Jiao, Ye Yang, Maojie Yuan, *et al.*, "Coke deposition mechanisms of propane dehydrogenation on different sites of Al2O3 supported PtSn catalysts," *Chemical Synthesis*, vol. 5, no. 1, p. 19, 2025. DOI: 10.20517/cs.2024.43. [Online]. Available: http://dx.doi.org/10.20517/cs.2024.43.

[47] Z. Shakor, A. Alasseel, and E. Al-Shafei, "The structure of deposited coke on hydrocracking and reforming catalysts: Coke deactivation and kinetics," *Canadian journal of chemical engineering*, vol. 102, no. 8, pp. 2876–2891, 2024, Place: Hoboken, USA Publisher: John Wiley & Sons, Inc, ISSN: 0008-4034. DOI: 10.1002/cjce.25222.

[48] P. N. Dwivedi and S. N. Upadhyay, "Particle-Fluid Mass Transfer in Fixed and Fluidized Beds," *Industrial & engineering chemistry process design and development*, vol. 16, no. 2, pp. 157–165, 1977, Publisher: American Chemical Society, ISSN: 0196-4305. DOI: 10.1021/i260062a001.

[49] C. L. Yaws, "Yaws' Critical Property Data for Chemical Engineers and Chemists," Publisher: Knovel, ISSN: N/A. [Online]. Available: https://app.knovel.com/hotlink/itble/rcid:kpYCPDCECD/id:kpYCPDCECD/yaws-critical-property/yaws-critical-property.

[50] S. b. A. Design Institute for Physical Properties, "DIPPR Project 801 - Full Version," Publisher: Design Institute for Physical Property Research/AIChE, ISSN: N/A. [Online]. Available: https://app.knovel.com/hotlink/itble/rcid:kpDIPPRPF7/id:kpDIPPRPF7/dippr-project-801-full/dippr-project-801-full.

[51] L. Holzer, P. Marmet, M. Fingerle, A. Wiegmann, M. Neumann, and V. Schmidt, *Tortuosity and Microstructure Effects in Porous Media : Classical Theories, Empirical Data and Modern Methods* (Springer Series in Materials Science, 333), 1st ed. 2023. Cham: Springer International Publishing, 2023, ISBN: 3-031-30477-2. DOI: 10.1007/978-3-031-30477-4.

[52] *SpringerMaterials – properties of materials*. [Online]. Available: https://materials.springer.com/ (visited on 06/18/2025).

[53] *Magnesium Aluminate Crystal Substrate, MgAl2O4 or Spinel | Stanford Advanced Materials*, en. [Online]. Available: https://www.samaterials.com/crystal-substrates/2423-magnesium-aluminate-crystal-substrate.html (visited on 06/18/2025).

A. Appendix

The Mears criterion can be defined accordingly [30]:

$$MR = \frac{r_{obs} Rn}{k_c C_b} \tag{A.1}$$

The mass transfer coefficient for Re>0.01 in packed beds can be described accordingly [48]:

$$k_c = \frac{\epsilon}{Sc^{2/3}} \left(\frac{0.765}{Re^{0.82}} + \frac{0.365}{Re^{0.386}}\right) \tag{A.2}$$

$$Re = \frac{d_p \nu \rho_g}{\mu_g} \tag{A.3}$$

$$Sc = \frac{\mu_g}{\rho_g D_{AB}} \tag{A.4}$$

The diffusion coefficient for a binary solution with O_2 in Ar can be calculated accordingly [49]:

$$D_{AB} = (0.0959 + 0.0007T + 9.25e^{-7}(T^2)) \tag{A.5}$$

The Ar viscosity can be calculated according to[50]:

$$\mu_g = \frac{9.2121e^{-7} \cdot T^{0.60529}}{1 + (\frac{83.24}{T})} \tag{A.6}$$

The Weisz Prater and effective diffusivity can be described as follows [30]:

$$MR = \frac{r_{obs} R^2}{D_e C_b} \tag{A.7}$$

$$D_e = \frac{D_{AB} \epsilon_p}{\tau} \tag{A.8}$$

The tortuosity can be described according to the Bruggeman equation for packed beds [51]:

$$\tau^2 = \epsilon_p^{-1/2} \tag{A.9}$$

The particle porosity is given by:

$$\epsilon_p = \frac{V_{pores}}{V_{pores} + \frac{1}{\rho_{cat}}} \tag{A.10}$$

Table A.1: Pore volumes derived from BET analysis and material density for the Al_2O_3 and $MgAl_2O_4$ supports

	Al_2O_3	$MgAl_2O_4$
V_{pores} ($cm^3\,g^{-1}$)	0.48	0.74
ρ_{cat} ($g\,cm^{-3}$)	3.67 [52]	3.61 [53]

B. Appendix

Mesh independence test:

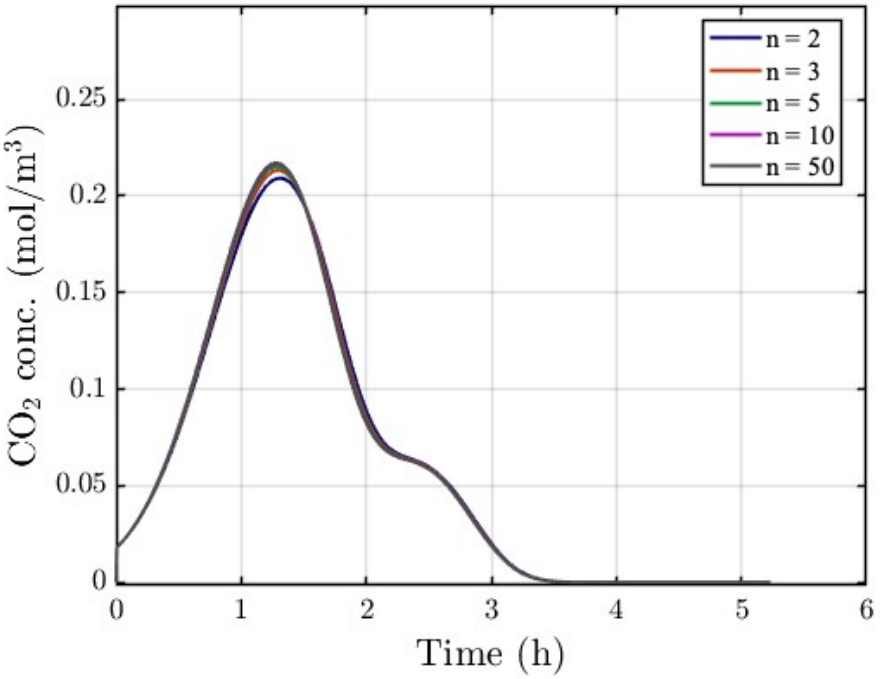

Figure B.1: Model CO_2 concentration at reactor outlet at different mesh discretizations for Pt/Al_2O_3

Table B.1: Mesh independence test results at reactor outlet at different mesh discretizations for Pt/Al_2O_3.

Number of nodes	Outlet CO_2 concentration at C_{max} (mol m^{-3})	Relative change at C_{max} (%)	Relative change of mean CO_2 conc. (%)
10	0.2164	–	–
20	0.2167	0.1449	0.0184
30	0.2168	0.0415	0.0086
40	0.2170	0.0725	0.0243
50	0.2170	0.0030	0.0123

Model solution using 20 nodes displays a relative change below 1%.

C. Appendix

Gas chromatogram of extract:

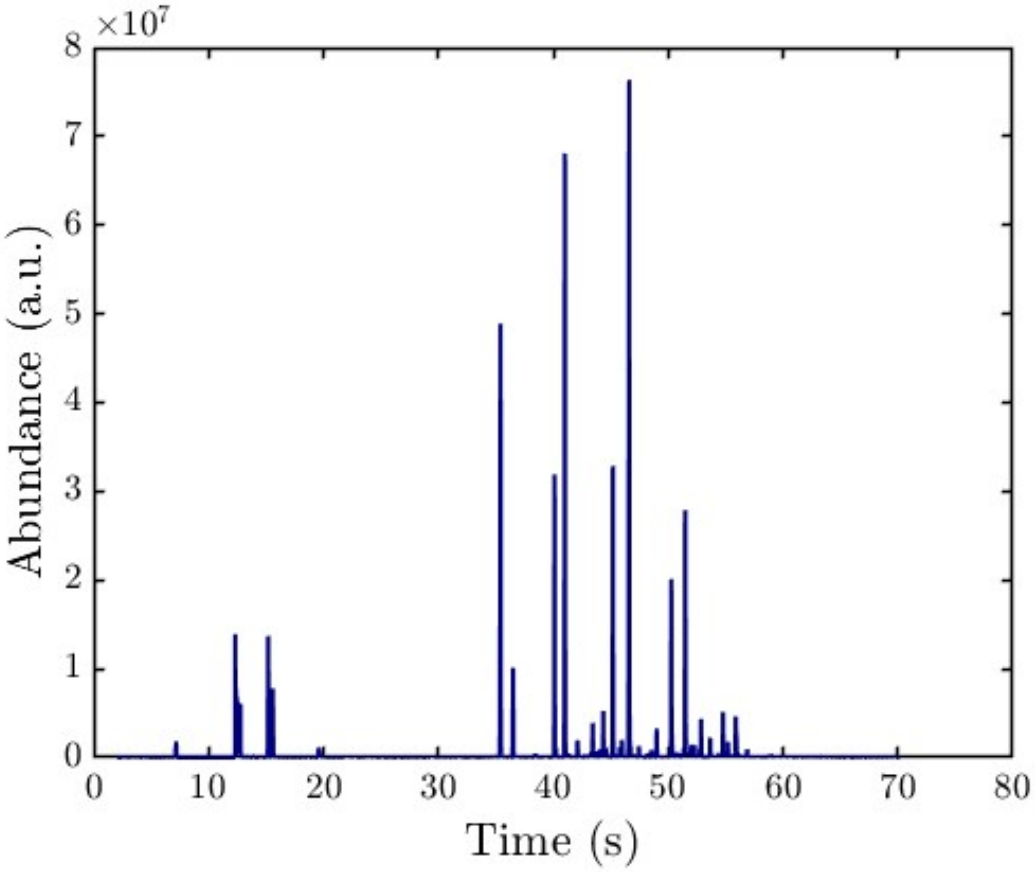

Figure C.1: Total Ion Chromatogram of extract

D. Appendix

Deconvolution of O_2 signals for Pt/Al_2O_3 and $Pt/MgAl_2O_4$:

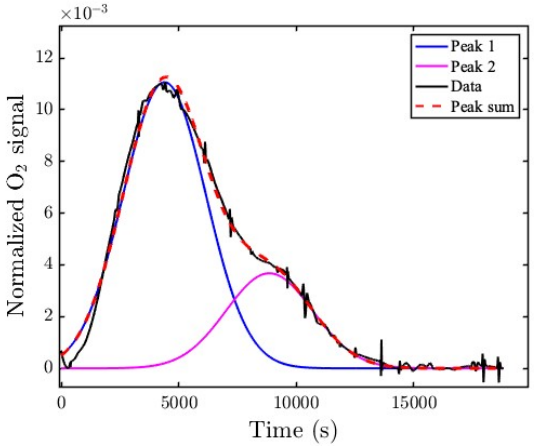

Figure D.1: O_2 deconvolution for Pt/Al_2O_3

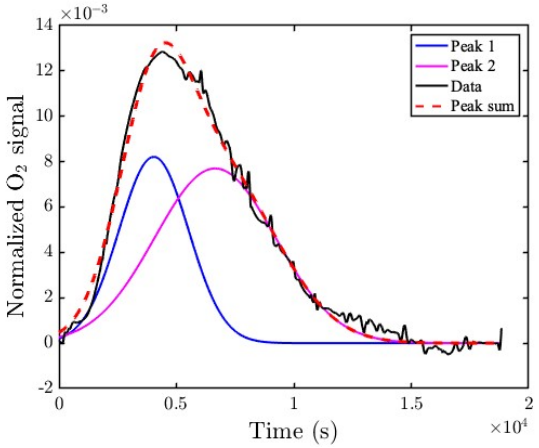

Figure D.2: O_2 deconvolution for $Pt/MgAl_2O_4$

E. Appendix

Full TGA profiles:

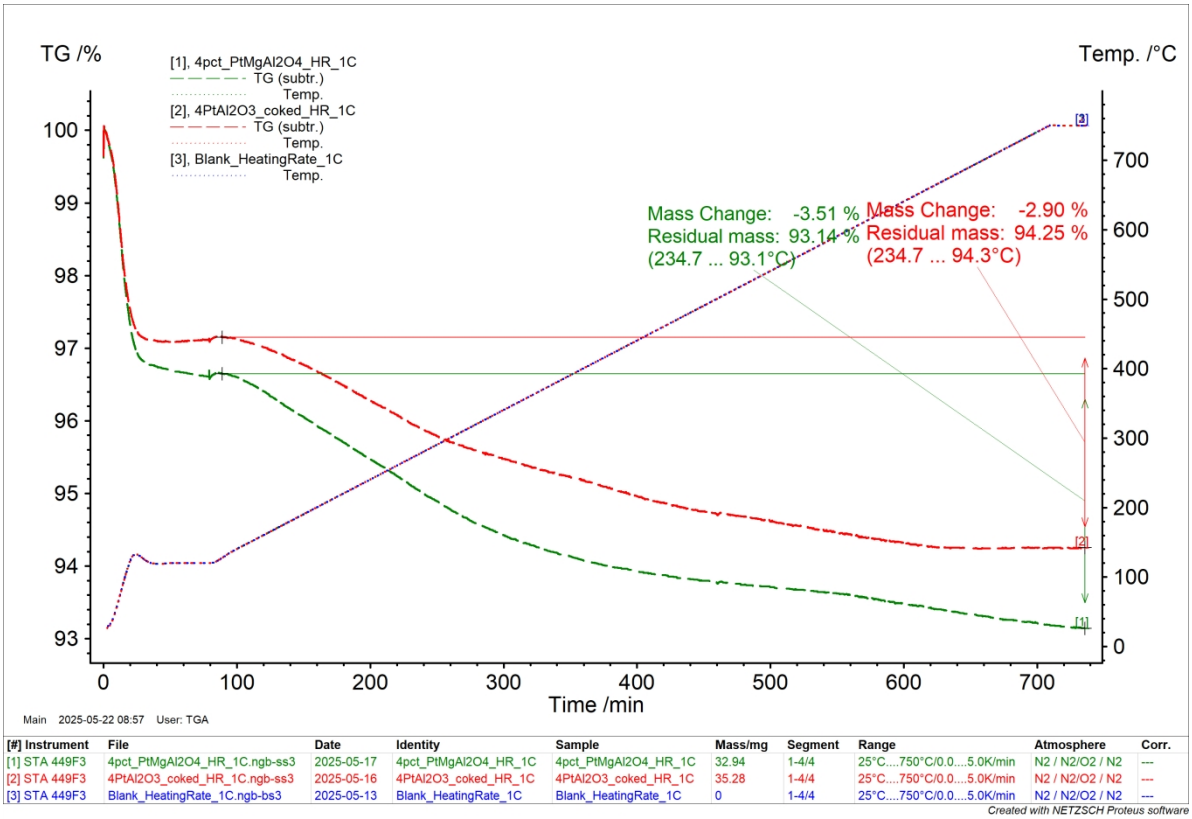

[#] Instrument	File	Date	Identity	Sample	Mass/mg	Segment	Range	Atmosphere	Corr.
[1] STA 449F3	4pct_PtMgAl2O4_HR_1C.ngb-ss3	2025-05-17	4pct_PtMgAl2O4_HR_1C	4pct_PtMgAl2O4_HR_1C	32.94	1-4/4	25°C....750°C/0.0....5.0K/min	N2 / N2/O2 / N2	---
[2] STA 449F3	4PtAl2O3_coked_HR_1C.ngb-ss3	2025-05-16	4PtAl2O3_coked_HR_1C	4PtAl2O3_coked_HR_1C	35.28	1-4/4	25°C....750°C/0.0....5.0K/min	N2 / N2/O2 / N2	---
[3] STA 449F3	Blank_HeatingRate_1C.ngb-bs3	2025-05-13	Blank_HeatingRate_1C	Blank_HeatingRate_1C	0	1-4/4	25°C....750°C/0.0....5.0K/min	N2 / N2/O2 / N2	---

Figure E.1: TGA of spent Pt/Al_2O_3 (red curve) and $Pt/MgAl_2O_4$ (green curve). Program used a heating rate of 1°C in Air atmosphere

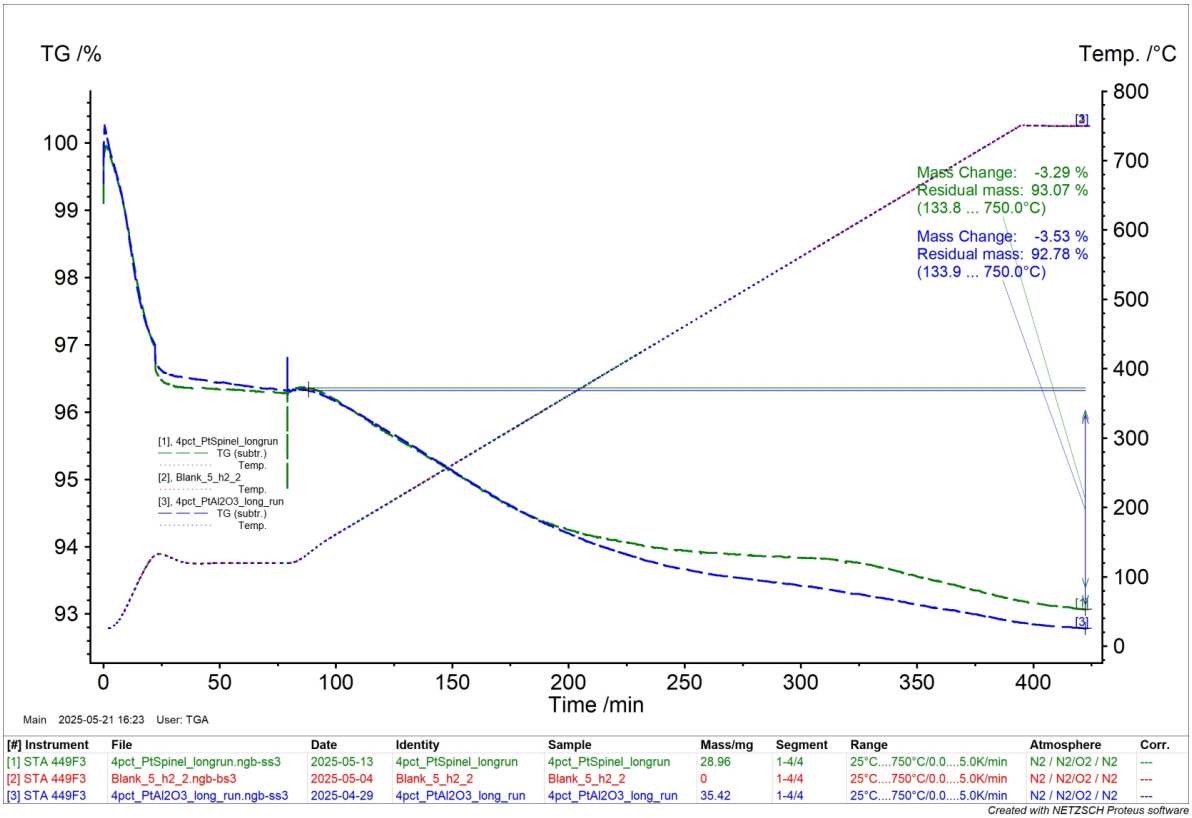

[#] Instrument	File	Date	Identity	Sample	Mass/mg	Segment	Range	Atmosphere	Corr.
[1] STA 449F3	4pct_PtSpinel_longrun.ngb-ss3	2025-05-13	4pct_PtSpinel_longrun	4pct_PtSpinel_longrun	28.96	1-4/4	25°C....750°C/0.0....5.0K/min	N2 / N2/O2 / N2	---
[2] STA 449F3	Blank_5_h2_2.ngb-bs3	2025-05-04	Blank_5_h2_2	Blank_5_h2_2	0	1-4/4	25°C....750°C/0.0....5.0K/min	N2 / N2/O2 / N2	---
[3] STA 449F3	4pct_PtAl2O3_long_run.ngb-ss3	2025-04-29	4pct_PtAl2O3_long_run	4pct_PtAl2O3_long_run	35.42	1-4/4	25°C....750°C/0.0....5.0K/min	N2 / N2/O2 / N2	---

Figure E.2: TGA of spent Pt/Al_2O_3 (blue curve) and $Pt/MgAl_2O_4$ (green curve). Program used a heating rate of 2°C in Air atmosphere

F. Appendix

FTIR of extracted and coked Pt/Al_2O_3.

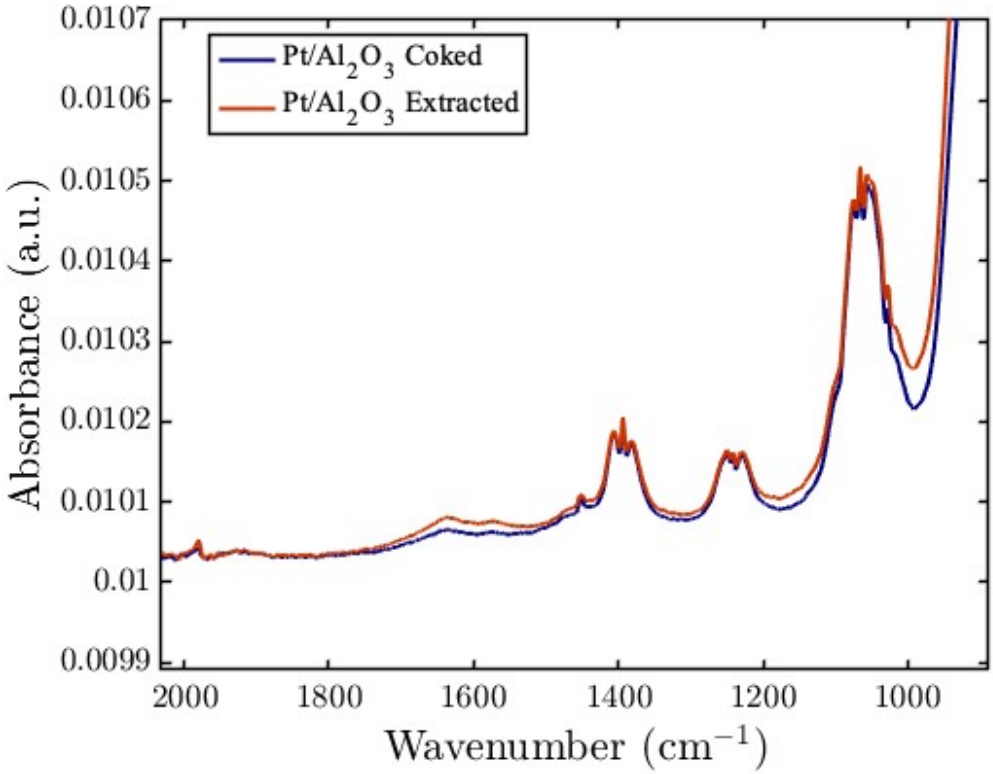

Figure F.1: FTIR of coked and extracted Pt/Al_2O_3